EXPLORING ELECTRON-SINK BEHAVIORS OF MOLECULAR ASSEMBLIES

by

Yume Mai

A thesis

submitted in partial fulfillment

of the requirements for the degree of

Master of Science in Chemistry

Boise State University

August 2021

BOISE STATE UNIVERSITY GRADUATE COLLEGE

DEFENSE COMMITTEE AND FINAL READING APPROVALS

of the thesis submitted by

Yume Mai

Thesis Title: Exploring Electron-sink Behaviors of Molecular Assemblies Date of Final

Oral Examination: 17 June 2021

The following individuals read and discussed the thesis submitted by student Yume Mai, and they evaluated the student's presentation and response to questions during the final oral examination. They found that the student passed the final oral examination.

Adam C. Colson, Ph.D.	Chair, Supervisory Committee
Eric Brown, Ph.D.	Member, Supervisory Committee
Matthew King, Ph.D.	Member, Supervisory Committee

The final reading approval of the thesis was granted by Adam C. Colson, Ph.D., Chair of the Supervisory Committee. The thesis was approved by the Graduate College.

DEDICATION

This thesis is dedicated to my parents and sister for their endless and unconditional love, support, patience, and kindness.

Cảm ơn ba mẹ, chị Duyên, anh Vinh, và William.

ACKNOWLEDGMENTS

I would like to sincerely thank Dr. Adam Colson, my committee chair, for your generous guidance and support. I am extremely grateful for the opportunity to contribute to this research. Without your persistent help and encouragement, this thesis would not have been possible. You've inspired me to become a creative and better scientist. I could not ask for a better research advisor and mentor for my master's study. Thank you for everything and for putting up with me!

To my committee members, Dr. Eric Brown and Dr. Matt King, thank you for your kind encouragement and insightful advice. I'm so thankful for all your help and willingness to listen to my endless complaints about (just almost) everything.

I would also like to acknowledge Dr. Joseph Dumais for training me on the NMR instrument. I'd like to extend my gratitude to Dr. Michael Callahan for keeping me on track with deadlines to graduate. Additionally, many thanks to the BSU Department of Chemistry and Biochemistry for the financial support provided through my teaching assistantship.

Finally, I'm forever grateful for the unconditional love and for all the sacrifices that my family has made for me. Without their support, I never expected in a million years to arrive at where I am today. Cảm ơn gia đình đã luôn ở cạnh, giúp đỡ, và nấu ăn cho con. Ba mẹ và chị Duyên luôn là niềm động lực lớn nhất để giúp con có được ngày hôm nay. To Christopher, thank you for always being so awesome and supportive. Your sense of humour may have rubbed off a little bit, but I'm still the funny one.

ABSTRACT

Metal carbonyl clusters, such as the $[Ni_{32}C_6(CO)_{36}]^{6-}$ anion, have been documented to display electron-sink phenomena. However, such large clusters suffer from inefficient yields due to their demanding and unreliable synthesis routes. To approach this obstacle, we investigated the electrochemical properties of $Fe_2(\mu\text{-}PPh_2)_2(CO)_6$, an organometallic complex known to experience a reversible two-electron transfer process. In this work, we report a modular synthetic strategy for expanding the electron-sink capacity of molecular assemblies by installing $Fe_2(\mu\text{-}PPh_2)_2(CO)_6$ redox mediators to arylisocyanide ligands. Specifically, the coordination of three $Fe_2(\mu\text{-}PPh_2)_2(CO)_6$ subunits to a trifunctional arylisocyanide ligand produces an electron-sink ensemble that can accommodate six electrons, exceeding the precedent benchmark $[Ni_{32}C_6(CO)_{36}]^{6-}$ anion. The redox mediators store electrons within quantized unoccupied frontier orbitals and act as individual quantum capacitors. Ultimately, we propose to modify the electrode surfaces with these redox mediators to examine the relationship between the electrode's mesoscopic structure and its macroscopic capacitance.

TABLE OF CONTENTS

LIST OF TABLES

LIST OF FIGURES

LIST OF ABBREVIATIONS

EC	Electrochemical Capacitor
EDLC	Electrochemical Double-Layer Capacitor
DOS	Density of States
HOMO	Highest Occupied Molecular Orbital
LUMO	Lowest Unoccupied Molecular Orbital
MCC	Metal Carbonyl Cluster
EIS	Electrochemical Impedance Spectroscopy
DC	Direct Current
CO	Carbonyl
NC	Isocyanide
TMANO	Trimethylamine N-Oxide
XRD	X-Ray Diffraction
NMR	Nuclear Magnetic Resonance
CV	Cyclic Voltammetry

CHAPTER 1: INTRODUCTION

1.1 Capacitors and Electrochemical Capacitors

A diverse spectrum of energy storage technologies is currently available, including chemical, mechanical, thermal, and electrochemical storage systems. Among these technologies, capacitors and supercapacitors are attracting substantial research interest in recent years.1-4 A capacitor is an electronic component that stores and modulates current flow. A typical capacitor consists of two conductive metal plates separated by an insulating or a dielectric medium. When an electrical potential is applied, positive and negative charges accumulate on opposite plates, creating an electric field across the dielectric. A charging current will flow until the voltage across both metallic plates equals the applied potential during the charging process. Due to the presence of the electric field, the capacitor blocks direct currents while storing the potential in the form of electrostatic charges. The potential difference across the capacitor depends on the work done by the applied voltage and the capacitor's ability to store charges or its capacitance. Capacitance (C) is defined as the ratio of accumulated charges (q) on the plates to the voltage (V) between them:

$$C = \frac{q}{V}$$

An electrochemical capacitor (EC) or supercapacitor is a new generation of energy storage device. ECs can bridge the performance gaps between electrostatic capacitors and rechargeable batteries. They manifest higher capacitance, quicker charging cycles, and

longer shelf life compared to conventional capacitors.[5,6] A simple EC can be assembled by inserting two metallic electrodes into an electrolyte solution. ECs are conventionally divided into two categories based on their storage mechanism: electrochemical double-layer capacitors and pseudocapacitors.

In electrochemical double-layer capacitors (EDLCs), the current flows from one electrode to the other, causing charge separation at each electrode-electrolyte interface due to physical ion adsorption and desorption. This electrostatic storage process is non-Faradaic, in which no charge transfer takes place across the electrode surfaces.[12,13] The capacitance of EDLCs depends heavily on the specific surface area of the electrodes. Porous carbon materials, carbide-derived carbons, and carbon-supported metal oxides have been tested as electrode materials for EDLCs.[6-8]

Alternatively, pseudocapacitors rely on the redox reactions at the surface of the electrodes. The pseudo-capacitive mechanism is a Faradaic process where electrons are transferred across the electrode interface via quick and reversible redox reactions of electrochemically active species.[12,13] Pseudo-capacitance depends intrinsically on the electrolyte choice as well as the material of the electrodes. Electroactive metal oxides (MnO_2, RuO_2, etc.), conductive polymers, and graphene derivatives have been the primary focus in developing electrode materials for pseudocapacitors.[9-11]

One of the critical challenges of the aforementioned bulk electrode materials for supercapacitors is their limited electrochemical tunability.[6-10] For example, crystallinity and electronic configurations are inherent factors that can impact capacitive performance. This thesis will explore the electrochemical capacitance phenomenon and discuss the electrochemical properties of discrete molecular species exhibiting quantized redox states.

Our objective is to investigate the relationship between the electrochemical density of states and the macroscopic capacitance using molecular-modified electrodes.

1.2 Mesoscopic Phenomenon and Quantum Capacitance

The energy storage ability of supercapacitors depends on the surface area of the electrodes. Nanomaterials have been studied and developed to maximize electrode surface area as well as their capacitive performance. However, upon miniaturization, the predictability of physical and electrochemical properties of materials becomes limited and elusive. At such diminutive scales, the material's conduction, resistance, capacitance, and charge transport mechanisms are not well understood.[14,15] Thus, from a theoretical standpoint, it becomes evident that an approximating model is urgently needed to bridge our knowledge gap regarding the intricate and perplexing nanoscale electrochemistry.

Inspired by the work of Bueno and colleagues, our studies were designed and constructed based on their mesoscopic physics model. The mesoscopic region is an intermediate region between the microscopic (molecular) and the macroscopic (bulk) scales. The mesoscopic realm provides essential information on the verge of purely quantum mechanical and purely classical regimes.[14,15] At the mesoscales, materials manifest complicated dynamics where quantum phenomena interfere with classical principles. Incidentally, electrochemical processes are essentially mesoscopic events. Depending on the charged state and the presence of chemical reactions, the electrochemical analysis can shift from classical mechanics to quantum mechanics or a combination of both.[14-17] Thus, by investigating and studying the mesoscopic electron transfer processes across molecular structures, we can extrapolate our conclusions to gain a deeper understanding of electrochemical properties at the nanoscales.

According to Bueno, the metallic electrode (electronic conductor) and the electrolyte solution (ionic conductor) supply electrons and ions, respectively. Fundamentally, the metallic and electrolytic environments only differ in terms of electronic or ionic statistics.[14-16] In a purely non-Faradaic charging process, distinguishable ions predominate, and Boltzmann approximation takes place. Therefore, variations in the electrical potential follow classical principles. On the other hand, indistinguishable electrons are the primary particles that govern Faradaic dynamics. In this case, Fermi-Dirac statistics is assumed, and fluctuations in the electrical potential follow quantum mechanics. Thus, the electrochemical Faradaic and non-Faradaic processes are intrinsically the same event at the mesoscales with different magnitudes of classical and quantum mechanics contributions.[14-16]

A mesoscopic circuit can be modeled as quantum capacitors assembled on a macroscopic electrode immersed in an electrolyte solution. The electrode and quantum capacitors are electronically coupled via quantum channels. The electrochemical capacitance can be defined as

$$\frac{1}{C_{\bar{\mu}}} = \frac{1}{C_i} + \frac{1}{C_q}$$

where $C_{\bar{\mu}}$ is the electrochemical capacitance, C_i is the ionic capacitance at the interface, and C_q is the quantum capacitance. The ionic capacitance term, C_i, is typically modeled as the double-layer capacitance. The quantum capacitance C_q is proportional to the electronic density of states (DOS) accessible at the interface due to perturbations made in the electrodes.[14,15] In the presence of faradaic activities, $1/C_q$ represents the energy difference between the frontier orbitals HUMO and LUMO of the mesoscopic system. As

such, the electrochemical capacitance term is a combination of ionic and quantized pseudo-capacitance elements.

1.3 Metal Carbonyl Clusters as Quantum Capacitors

Metal carbonyl clusters (MCCs) are organometallic complexes containing two or more transition metal centers stabilized by carbon monoxide (CO) ligands. Electron-sink compounds, such as MCCs, can reversibly store and release electrons when a potential is applied.[18-21] The $[Ni_{32}C_6(CO)_{36}]^{6-}$ carbide anion is considered a benchmark of electron-sink capacity in molecular materials.[22] The anion's cyclic voltammogram displays a five-electron transfer process with features of redox reversibility while retaining the original structure. However, such large clusters suffer from demanding synthesis and unpredictable yields, which hinders the advancement of MCCs as practical capacitor materials.[22-25] To address such obstacles, we propose to synthesize redox arrays via a modular synthetic approach and investigate their electrochemical capabilities.

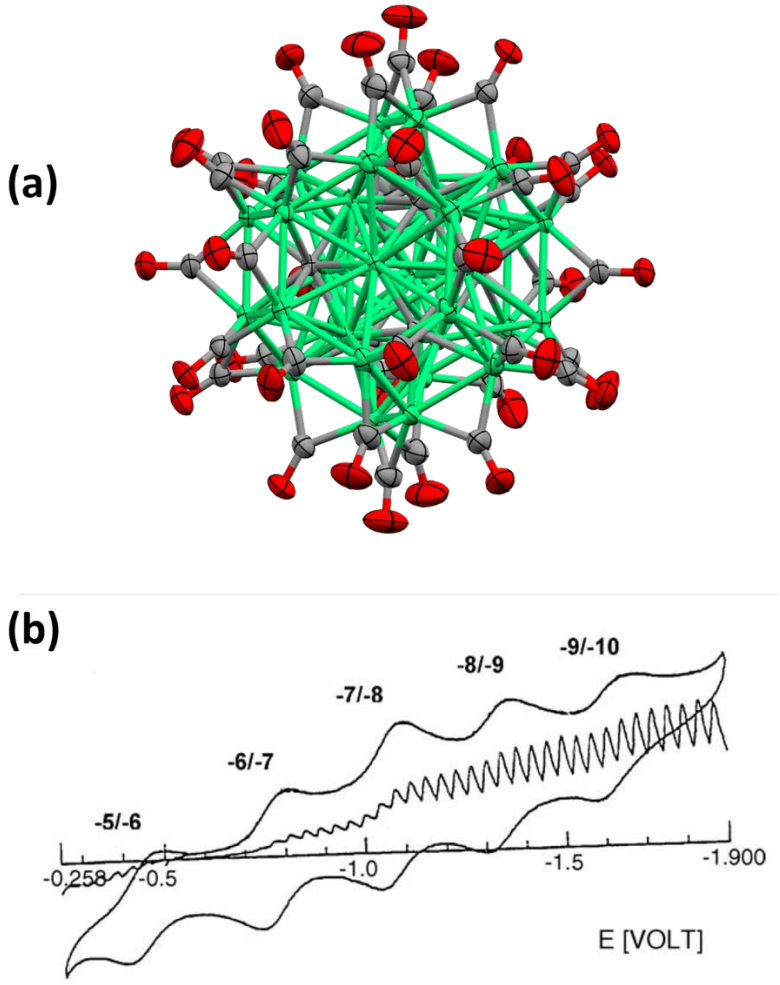

Figure 1. (a) Molecular structure of $[Ni_{32}C_6(CO)_{36}]^{6-}$ complex and (b) its cyclic voltammetry profile, which shows successive five-electron reduction steps.

The organometallic complex $Fe_2(CO)_6(\mu-PPh_2)_2$ (**1**) contains an iron–iron single bond, in which each iron atom is bound to two bridging phenylphosphido ligands and three terminal carbonyl ligands. The cyclic voltammogram of **1** suggests the occurrence of a reversible, two-electron reduction process. [26-28]

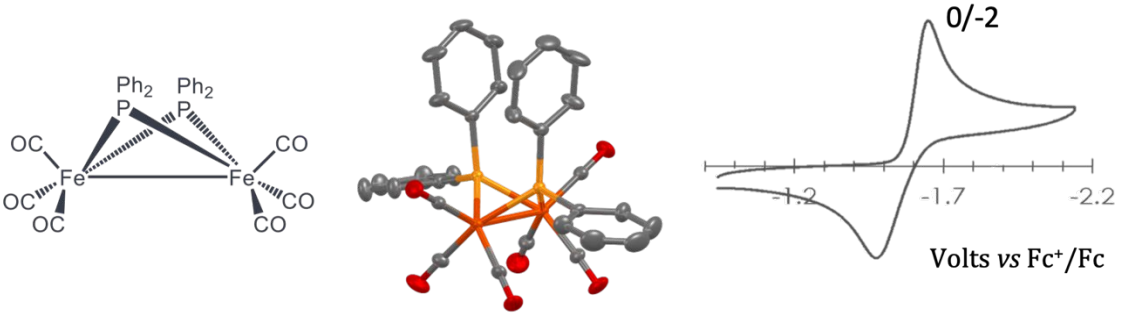

Figure 2. Fe_2P_2 structure and cyclic voltammogram. A two electron-reduction process is observed.

To further examine the electron-sink capacity of this redox mediator precursor, we prepared several derivatives of the **1**, in which one of the terminal carbonyls is replaced with an isolobal arylisocyanide analog. The cyclic voltammogram profile of the monosubstituted arylisocyanide derivative shows a reversible, two-electron transfer process similar to the parent subunit. However, there was a slight cathodic shift in the redox wave. Installation of two **1** subunits to a disubstituted arylisocyanide ligand results in an electron-reservoir conglomeration that can accommodate up to four electrons. With this experimental evidence, it was hypothesized that the installation of an additional **1** subunit to a trifunctional arylisocyanide ligand would result in an expanded electron-sink capacity (i.e., six electrons).

1.4 Electrochemical Impedance Spectroscopy (EIS)

Resistance is a measure of an electric circuit's opposition to the flow of a steady direct current (DC). *Impedance* is defined as the overall resistance that only occurs in AC circuits. In addition to resistance, impedance also includes the effects of inductance and capacitance due to the magnetic field and electrostatic charges, respectively.[29] The impedance (Z) complex number is often represented in Cartesian coordinates as

$$Z = R + jX$$

where the real component of the impedance is resistance (R), and the imaginary component is a combination of capacitance and inductance (X).[31,32]

Electrochemical impedance spectroscopy (EIS) is a sensitive method used to determine the double-layer capacitance and to examine electrode and complex interface processes.[30-33] EIS studies how an electrochemical system responds to an application of a sinusoidal voltage over a range of various frequencies. Impedance is determined by exciting an electrochemical cell with an AC potential and measuring the resulting current. The current response is a sinusoid at the same frequency as the excitation voltage but shifted in phase. The excitation signal as a function of time can be written as

$$E(t) = E_0 \sin(\omega t)$$

where E_0 is the amplitude of the voltage signal, ω is the angular frequency, and t is time.[31,32] The response signal I with amplitude I_0 shifted in phase ϕ can be written as

$$I(t) = I_0 \sin(\omega t + \phi)$$

The impedance (Z) can be expressed in terms of an impedance with magnitude Z_0 and a phase shift ϕ as

$$Z = \frac{E(t)}{I(t)} = Z_0 \frac{\sin(\omega t)}{\sin(\omega t + \phi)}$$

The results of the impedance measurements are often evaluated using the Nyquist plot or Bode plot.[31,32] The Nyquist plot shows the imaginary component of the impedance as a function of the real counterpart, whereas in the Bode plot, phase angles are plotted as a function of frequency. While both diagrams offer certain advantages, they contain the same information that can easily be extracted for different purposes. Our research group is interested in employing EIS to determine electrochemical parameters of electroactive

redox arrays, which will explicate the electrochemical interactions at the mesoscopic levels.

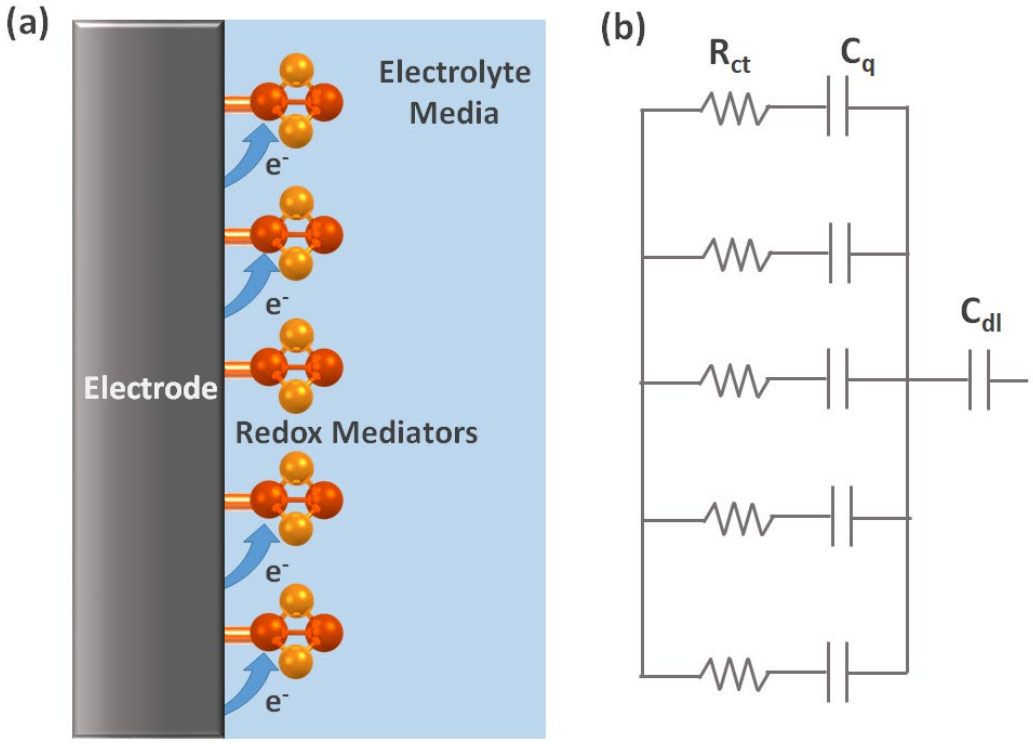

Figure 3. Schematic representation of an electrode surface modified with molecular redox mediators & circuit representation of the ensemble.

Redox mediators, such as **1** and its derivatives, accommodate electrons within the quantized unoccupied frontier molecular orbitals. Since these molecular orbitals represent quantized energy states, redox mediators act as individual quantum capacitors. In recent publications, Bueno and colleagues proposed a quantum RC electronic circuit model, in which the redox mediators are represented as circuit elements (**Figure 3**). In this model, each quantum capacitor is assembled on an electrode via quantum channels creating an ensemble of individual quantum point contact structures (or quantum dots).[14,15] An important implication of this model is that the total charge transfer resistance due to the electrolyte solution (R_{ct}), the double-layer capacitance (C_{dl}), and the quantum capacitance (C_q) can be experimentally quantified using EIS.

1.5 Thesis Overview

In this chapter, the Faradaic and non-Faradaic charge storage mechanisms have been introduced. Our research group is interested in studying the electron-sink behaviours of metal carbonyl clusters. We propose to use a modular synthetic approach to construct redox mediator arrays and examine their electrochemical features. The synthesis and structural characterization of a **1** derivative bearing trifunctional arylisocyanide ligand will be discussed in the following chapter. The electrochemical properties and optimized reduction conditions of **1** and its derivatives will be described. Lastly, this thesis will briefly outline the directions for future studies based on the results of this work.

CHAPTER 2. SYNTHESIS AND CHARACTERIZATION OF $C_{106}H_7Fe_6N_3O_{15}P_6$

2.1. Introduction

With the advancement of technological devices, there is a great demand for the research and development of materials with deliberate and predetermined properties. Phosphido-bridged transition metal complexes have been gaining research interests as promising avenues for technological applications, including electrochemical devices. The binuclear phosphido-bridged transition metal complex $Fe_2(CO)_6(\mu-PPh_2)_2$ (**1**) is considered the simplest form of metal carbonyl cluster (MCC). Our research group identified complex **1** as an ideal precursor for our studies, in which **1** was chosen due to its electron-sink behaviors, constituent elemental abundance, and simplistic structure.[34,35] Along with the PR_2 phosphido groups, the terminal carbonyl CO ligands enhance the stability of the diiron system due to the σ-donor and π-acceptor characteristics of CO ligands. In this context, electron-rich metal centers are stabilized by π-backbonding, where electrons are donated to the π^* orbitals reside on the carbon molecules.

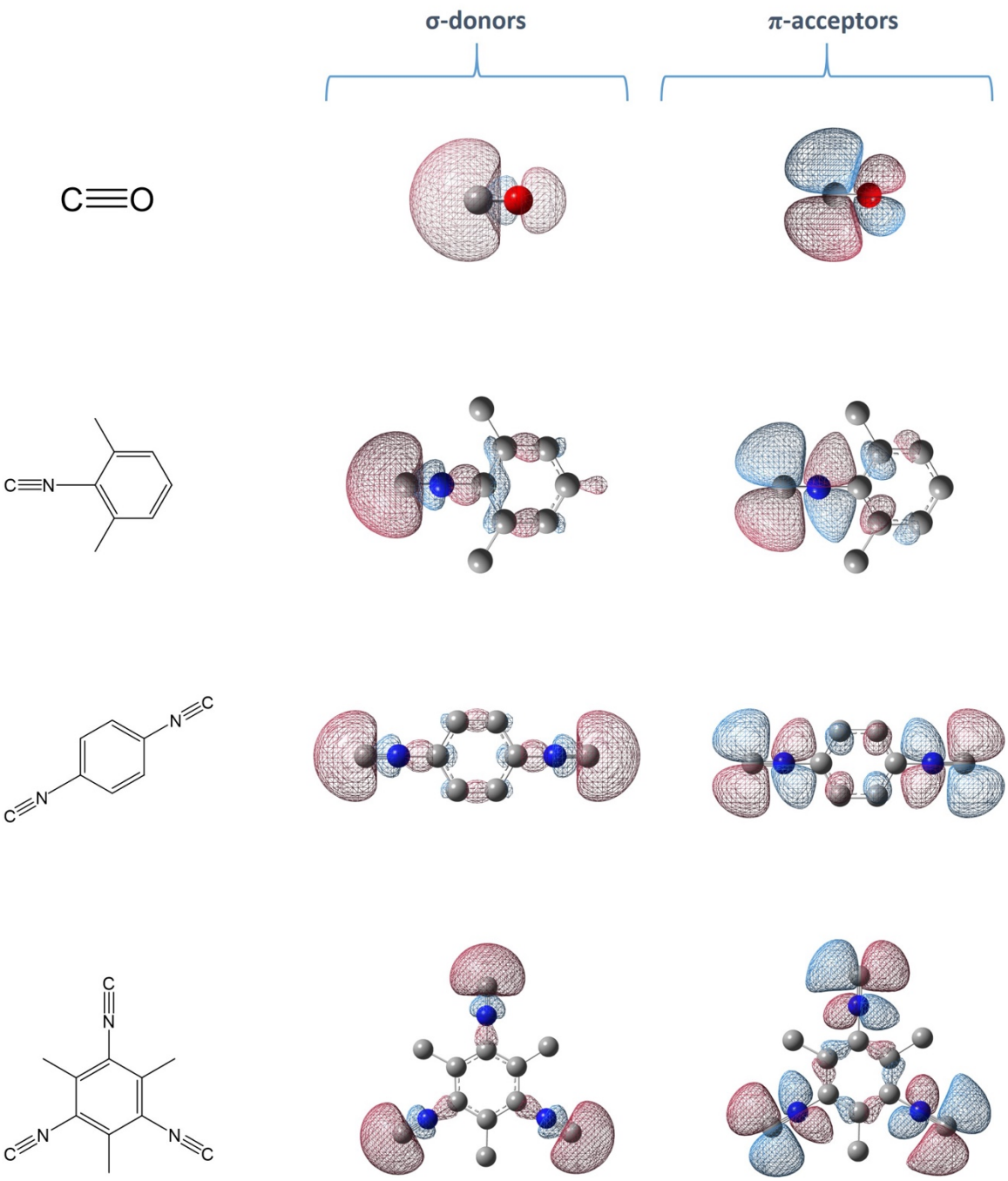

Figure 4. *σ*-donor and *π*-acceptor molecular orbitals of carbonyl and arylisocyanide ligands. Isocyanides are isolobal analogues of CO with similar steric properties.

The isocyanide N≡C functional group is a versatile surrogate to the carbonyl ligand, in which isocyanide is proven to form stable transition metal complexes analogous to metal carbonyls.[36] Notably, empirical studies classified isocyanides as stronger *σ*-

donors and weaker π-acceptors compared to CO ligands.[37,38] Such similarities in bonding properties between isocyanide and carbonyl ligands are attributed to their analogous molecular orbital architectures and steric profiles (**Figure 4**). As part of our ongoing studies to systematically expand the electron-sink capacity of molecular redox arrays, our research group has been exploring the chemistry of arylisocyanides for use as alternatives to carbonyl ligands. Specifically, we have successfully prepared two derivatives of **1**, in which one of the terminal carbonyl ligands was replaced with an aromatic ligand bearing one or two isocyanide functional groups (**Figure 5**).

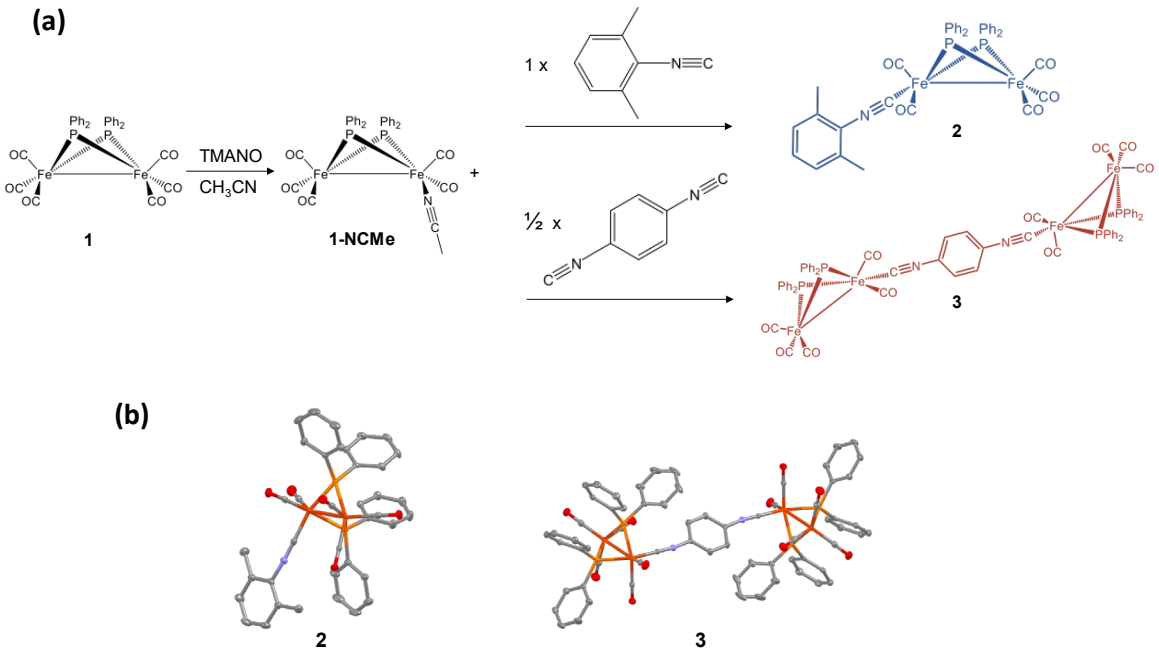

Figure 5. (a) Modular synthetic strategy for preparing electroactive assemblies bearing one (2) and two (3) $Fe_2(CO)_6(\mu-PPh_2)_2$ fragments tethered to arylisocyanide ligands. (b) Molecular structure of 2 and 3. Hydrogen atoms are omitted for clarity.

The monosubstituted and disubstituted derivatives were prepared via a series of chemical reactions as shown in **Figure 5a**. Accordingly, treatment of **1** with trimethylamine N-oxide (TMANO) causes one of the terminal CO ligands to displace via

the decarbonylation reaction mechanism. The intermediate(**1–NCMe**) from this reaction was subsequentially combined with 2-isocyano-1,3-dimethylbenzene and 1,4-diisocyanobenzene to form **2** and **3**, respectively. Encouraged by the successful synthesis of **2** and **3**, we have adapted the described derivatization procedure to prepare **4**, a derivative of **1** bearing three arylisocyanide functional groups as outlined in **Scheme 1**. In this chapter, the synthesis of the 2,4,6-triisocyanomesitylene ligand and the electroactive derivative **4** is discussed. Also reported herein is the structural characterization of **4** using IR spectroscopy and x-ray crystallography.

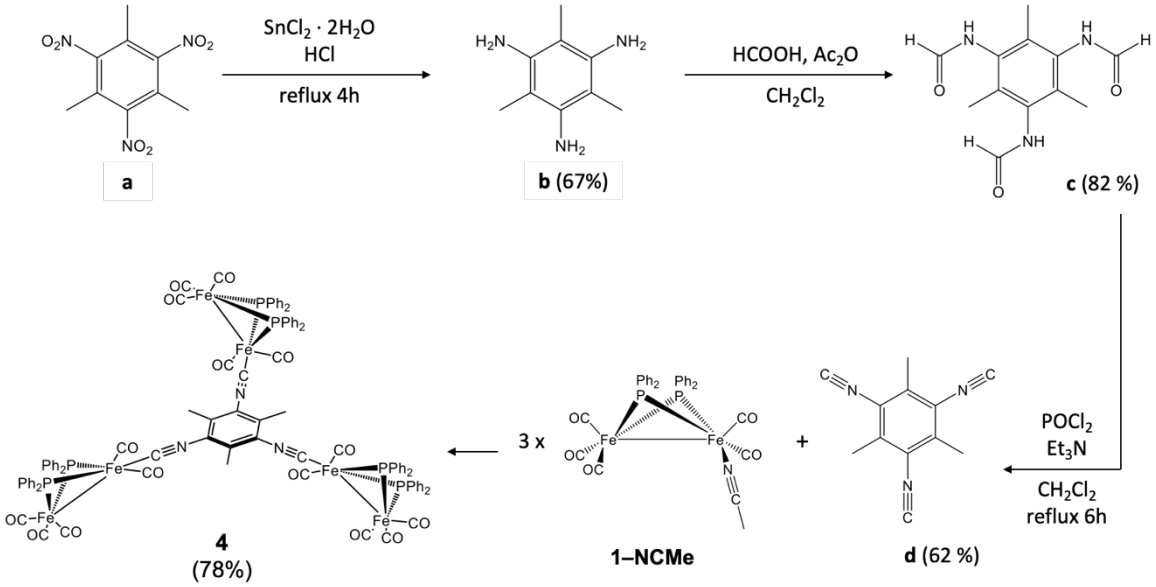

Scheme 1. Synthesis of electroactive assemblies bearing three Fe2(CO)5(μ −PPh2)2 fragments appended to 2,4,6-triisocyanomesitylene ligand.

2.2. Experimental

General considerations

All reactions were performed using standard Schlenk and vacuum-line techniques under inert nitrogen atmosphere. Nitrogen gas was purified by passing through columns of activated copper catalyst (BASF PuriStar R3-11G) and molecular sieves (RCI-DRI

13X). Except where indicated, all chemical reagents were used as received without further purification. All solvents were dried according to standard procedures. Glassware was dried in an oven at 130 ℃, assembled while hot, and was allowed to cool under reduced pressure. 2,4,6-trinitromesitylene was prepared according to published procedure.

Infrared spectra were collected using Thermo Scientific Nicolet iS5 FT-IR spectrometer equipped with a 0.2 nm BaF_2 liquid cell. ^{1}H and ^{13}C NMR spectra were obtained using a 600 MHz Bruker AVANCE III spectrometer.

Synthesis of triaminomesitylene (b)

$SnCl_2 \cdot 2H_2O$ (21.2288 g, 94.1 mmol) was dissolved in 79 mL HCl, followed by the addition of 2,4,6-trinitromesitylene (1.9932 g, 7.81 mmol). The reaction mixture was magnetically stirred and heated under reflux for 4 h. Once the solution turned yellow and clear, the flask was removed from heat and allowed to cool to room temperature. The reaction mixture was made basic using KOH until a pH of 11 was achieved. The alkaline mixture was gently heated until the solution became clear. Upon cooling to room temperature, a white crystalline precipitate formed, which was filtered and discarded. The filtrate was extracted with CH_2Cl_2. The organic layer was dried by anhydrous $MgSO_4$ and the organic solvent was removed under reduced pressure to obtain fine, yellow powder. The crude product was purified by crystallization using MeOH. Yellow crystalline product (0.8591 g, 66.6%) was collected and dried under vacuum for a few hours. IR (ATR, cm^{-1}), 3390 (m), 3340 (m), 3240 (w), 2900 (w), 2860 (w), 1620 (s), 1600 (s), 1450 (s), 1120 (s). ^{1}H NMR (600 MHz, $CDCl_3$), δ 1.99 (s, 9 H), 3.488 (s, 6 H), which are consistent with literature values.

Synthesis of triformamidomesitylene (c)

Formic acid (4.97 mL, 131.6 mmol) was combined with acetic anhydride (99 %, 4.48 mL, 47.0 mmol) and magnetically stirred at 0 ℃ for 20 min. Triaminomesitylene (2.0708 g, 12.5 mmol) was dissolved in 70 mL dried CH_2Cl_2 and was slowly introduced to the reaction flask. The combined mixture was magnetically stirred at 0 ℃ for 20 min and then was stirred for an additional 24 h at 25 ℃, after which the mixture thickened and became pale yellow and cloudy. Solvents were removed under reduced pressure, and the pale-yellow solid product was obtained. The product was suspended in cold MeOH, filtered, and washed with additional cold MeOH. The obtained white powdery product was dried under vacuum for 1 h. Yield: 2.5501 g (81.6%). IR (ATR, cm^{-1}), 3174 (w), 3013 (w), 2913 (w), 1651 (ν_{CO}, s), 1587 (m), 1533 (m), 1495 (m). ^{13}C NMR (600 MHz, DMSO-d6), δ 14.2, 131.2, 132.3, 159.6. ^{1}H NMR is complicated by the known distribution of *cis* and *trans* tautomeric isomers. Anal.Calcd for $C_{12}H_{15}N_3O_3$: C, 57.82; H, 6.07; N, 16.86. Found: C, 57.67; H, 6.11; N, 16.76.

Synthesis of triisocyanomesitylene (d)

Triformamidomesitylene (1.0204 g, 4.09 mmol) and triethylamine (5 mL, 35.9 mmol) were combined in 100 mL of dried CH_2Cl_2. The content was magnetically stirred while $POCl_3$ (2.2596 g, 14.7 mmol) was added dropwise to the reaction flask, whereupon the mixture slowly changed from cloudy yellow to a hazy orange solution. The reaction flask was heated at reflux at 44 ℃ for 6 h and was stirred for an additional 24 h at 25 ℃. The reaction mixture was quenched with sodium bicarbonate solution and the bi-phasic mixture was filtered to remove insoluble impurities. The aqueous layer was extracted with CH_2Cl_2, and the organic extract was dried by anhydrous $MgSO_4$. The crude solid was

purified by sublimation at 80 ℃ at 9.7 torr. Yield: 0.4934 g (61.8%). IR (ATR, cm^{-1}), 2111(ν_{NC}, s), 1669 (w), 1579 (w), 1445 (w), 1386 (m), 1067 (m). ^{1}H NMR (600 MHz, $CDCl_3$), δ 2.57 (s, 9 H). ^{13}C NMR (600 MHz, DMSO), δ 15.9, 133.4, 170.5, *ipso* carbon was not observed.

Synthesis of $Fe_2(CO)_6(\boldsymbol{\mu}-PPh_2)_2$ (1)

Adapted from published literature procedure.[26,39-40] Fe_3CO_{12} (10.13 g, 20.11 mmol) and PPh_2H (7.49 g, 40.22 mmol) was combined in 150 mL toluene. The mixture was magnetically stirred and heated at reflux for 72 h. Organic solvents were removed under vacuum upon cooling to room temperature. The crude product was purified by crystallization using hexanes. Shiny, brown crystalline product was collected and dried under reduced pressure for a few hours. Yield: 8.008 g (61%). IR spectroscopy (toluene, cm^{-1}), ν_{CO} 2055 (m), ν_{CO} 2015 (s), ν_{CO} 1991 (m), ν_{CO} 1964 (m). IR spectroscopic data is consistent with literature values.[26,39-40]

Synthesis of 1–NCMe

Adapted from published literature procedure.[26,39-40] Fe_2P_2 (2.0137 g, 3.10 mmol) was dissolved in 70 mL of dried CH_3CN, followed by addition of TMANO (1.1750 g, 15.7 mmol). The cloudy, orange reaction mixture was magnetically stirred at 50 ℃ for 2 h, then stirred for an additional 30 min at 25 ℃. Organic solvents were removed under reduced pressure. The solid product was suspended in CH_2Cl_2 and filtered through a pad of alumina to remove insoluble impurities with additional CH_2Cl_2. The filtrate was collected and dried under reduced pressure. The product was used for following steps without further purification. Yield: 1.73 g (84.3%). IR (CH_3CN, cm^{-1}), ν_{CN} 2056 (w), ν_{CO} 2022 (m), ν_{CO} 1980 (s), ν_{CO} 1943 (m), ν_{CO} 1921 (w).

Synthesis of 4

1–NCMe (1.70 g, 0. 534 mmol) was dissolved in 100 mL of dried THF, followed by addition of triisocyanomesitylene (0.1394 g, 0.712 mmol). The content was magnetically stirred for 3 h at 50 ℃, then stirred for an additional 24 h at 25 ℃. Organic solvents were removed under reduced pressure. The crude product was suspended in CH_2Cl_2 and filtered through a silica plug. The filtrate was dried, and the remaining solid was extracted in hot CH_3CN then slowly cooled to 0℃ for a few hours. The precipitate was filtered to obtain the fine, yellow powder product. The final product was purified by crystallization using toluene and IPA layer diffusion. Yield: 1.1426 g (78%). IR (CH_2Cl_2, cm^{-1}), ν_{CN} 2087 (m, br), ν_{CO} 2022 (s), ν_{CO} 1988 (s), ν_{CO} 1953 (s). ^1H NMR (600 MHz, $CDCl_3$), δ 1.68 (s, 9 H), 6.69 (t, 12 H), 6.80 (t, 6 H), 7.15 (m, 12 H), 7.16 (m, 19 H), 7.60 (m, 12 H). Anal. Calcd for $C_{106}H_7Fe_6N_3O_{15}P_6$•0.4 C_7H_8: C, 58.27; H, 3.47; N, 2.00. Found: C, 58.17; H, 3.41; N, 2.06.

Table 1. X-ray data collection and refinement parameters for complex 2 – 4

Compound	**2**	**3**	**4**
Formula	$C_{38}H_{29}Fe_2NO_5P_2$	$C_{66}H_{44}Fe_4N_2O_{10}P_4$	$C_{109.5}H_{81}Fe_6N_3O_{15}P_6$
Formula weight	753.26	1372.31	2199.69
Temperature (K)	100	100	100
Crystal system	monoclinic	monoclinic	triclinic
Space group	$P2_1/n$	$P2_1/n$	P-1
a (Å)	10.3290(9)	11.8076(10)	17.1726(18)
b (Å)	15.2946(15)	15.2235(14)	17.5708(18)
c (Å)	22.037(2)	19.0754(16)	40.208(4)
α (deg)	90	90	81.352(5)
β (deg)	94.996(3)	100.840(3)	80.677(5)
γ (deg)	90	90	88.014(4)
Volume ($Å^3$)	3468.1(6)	3367.7(5)	11835(2)
Z	4	2	4
density ($g/cm^{3)}$	1.443	1.353	1.235
abs coeff (mm^{-1})	0.973	0.995	6.971
F(000)	1544.0	1396.0	4500.0
Crystal size (mm)	0.27 × 0.16 × 0.1	0.6 × 0.17 × 0.15	0.31 × 0.21 × 0.05
λ (MoKα) (Å)	0.71073	0.71073	1.54178[a]
2θ range (deg)	4.516 to 55.104	5.716 to 61.014	4.502 to 80.176
reflns (coll)	119149	117989	96822
reflns (unique)	7981	10269	14361

Data/restraints/parameters	7981/0/435	10269/0/388	14361/4919/2437
GOF (on F^2)	1.038	1.046	1.080
Final R indexes [$I \geq 2\sigma(I)$]	$R_1 = 0.0277$ $wR_2 = 0.0637$	$R_1 = 0.0295$ $wR_2 = 0.0739$	$R_1 = 0.1054$ $wR_2 = 0.2456$
Final R indexes [all data]	$R_1 = 0.0370$ $wR_2 = 0.0677$	$R_1 = 0.0397$ $wR_2 = 0.0784$	$R_1 = 0.1260$ $wR_2 = 0.2569$
Largest diff. peak/hole (e $Å^{-3}$)	0.44/-0.21	0.51/-0.26	1.38/-0.78

[a] CuKα radiation

2.3 Results and Discussion

Synthesis of organic ligand

In pursuing our interest in expanding the electron-sink capacity of molecular materials, we sought to identify a suitable triisocyanide aromatic core capable of binding to our chosen electroactive subunit **1**. In previous pilot experiments, we prepared 1,3,5-triisocyanobenzene via the dehydration of 1,3,5-triformamidobenzene. Unfortunately, 1,3,5-triisocyanobenzene showed poor thermal stability, in which the decomposition reaction proceeds steadily at 35℃. This thermal instability led to challenges in the purification of 1,3,5-triisocyanobenzene as well as the coordination of the ligand to **1**.

Given the preceding limitations, we hypothesized that the presence of additional methyl groups on the benzene ring would afford an improvement in the stability of the trifunctional arylisocyanide core. Accordingly, we have designed a methodology for the synthesis of 2,4,6-triisocyanomesitylene (**d**) using inexpensive reagents (**Scheme 1**). Before undertaking this study, this organic ligand has not been reported in the literature. However, just recently, Hsu and colleagues published their preparation of 2,4,6-triisocyanomesitylene using a procedure similar to that outlined in this work.[41]

The triisocyanide derivative **d** was obtained through a four-step procedure starting with mesitylene. Nitration of mesitylene using nitric acid and concentrated sulfuric acid at 0℃ produces the 2,4,6-trinitromesitylene (**a**) intermediate, which was then reduced to yield 2,4,6-triaminomesitylene (**b**). Preliminary work carried out indicated that the reduction of **a** was particularly exacting and unpredictable. Previously, $FeCl_3 \bullet 6H_2O$ and hydrazine monohydrate were employed to reduce the nitro groups on the mesitylene ring. While producing the desired product **a**, this reduction methodology required refluxing the

mixture for over 12h. In addition, the yields of the reaction were inconsistent (10–79%), and a combination of partially reduced products and hydrochlorate products were present as impurities. Despite attempting different experimental conditions, improved results could not be obtained. We speculate that the presence of weakly electron-donating methyl groups increased the electron density and altered the reactivity of the molecule, which led to incomplete reduction of nitro functionalities.

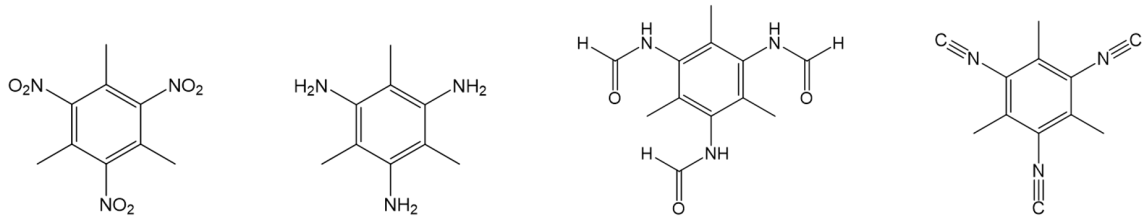

Figure 6. Structure of a – d.

We then examined the reduction of **a** using a combination of $SnCl_2 \cdot 2H_2O$ and concentrated hydrochloric acid. While this combination was very efficient in reducing the nitro groups to primary amines, the isolation of the desired product was complicated by the regeneration of $SnCl_2$ upon neutralization during workup. Therefore, we have established optimized conditions for the isolation and purification of **b**. Specifically, the reaction time was reduced to four hours, and the mixture was made basic using a solution of KOH until a pH of 11 was achieved. Additionally, we found that the $SnCl_2$ byproduct can be easily isolated and filtered upon recrystallization. Under these optimized conditions, **b** was obtained in good yields (66.6%) and was purified via crystallization using MeOH.

The formylation reaction to convert **b** to 2,4,6-triformamidomesitylene (**c**) proceeded at mild conditions and was very efficient (82%). The 2,4,6-triisocyanomesitylene ligand (**d**) was successfully prepared via the dehydration of **c** using triethylamine (Et_3N) and phosphoryl chloride ($POCl_3$). It should be noted that **d** arylisocyanide core is appreciably more stable compared to the 1,3,5-triisocyanobenzene precursor, in which **d** was efficiently purified by sublimation at 80℃ without experiencing decomposition.

The products **b – d** were characterized by IR, ^{1}H NMR, ^{13}C NMR, elemental analysis, and mass spectrometry (Experimental section). Interestingly, the ^{1}H NMR spectrum of **c** is complicated by the distribution of *cis* and *trans* tautomeric isomers of the formamide functional groups.[42] Additionally, substantial peak overlapping encumbered the spectral assignment of the ^{1}H spectrum of **c**. The ^{1}H NMR spectrum of **d** features a singlet 2.57 ppm, and the IR spectrum shows a strong NC stretching frequency at 2111 cm^{-1}. The ^{13}C NMR result features three peaks at 15.9, 133.4, and 170.5 ppm, in which the *ipso* carbon was not observed. The spectral data, mass spectrometry and elemental analysis results confirmed the formulation of **d** using the proposed synthetic route.

Synthesis and characterization of trimer

Given the success of the above reaction, we explored the coordination of **d** to the redox-active subunit using a similar procedure to prepare **2** and **3**. Accordingly, the acetonitrile-coordinated intermediate **1–NCMe** was combined with **d** to produce the corresponding isocyanide-appended complex **4** bearing three $Fe_2(CO)_6(\mu-PPh_2)_2$ fragments (**Scheme 1**). Upon workup, the obtained product was a glassy, amorphous orange solid. Due to its sterically hindered structure and the presence of multiple

functional groups, purification by crystallization of **4** was particularly challenging. We speculated that a bulky solvent system is required to fill in the large void spaces around the aromatic core in order to crystallize the desired product efficiently.

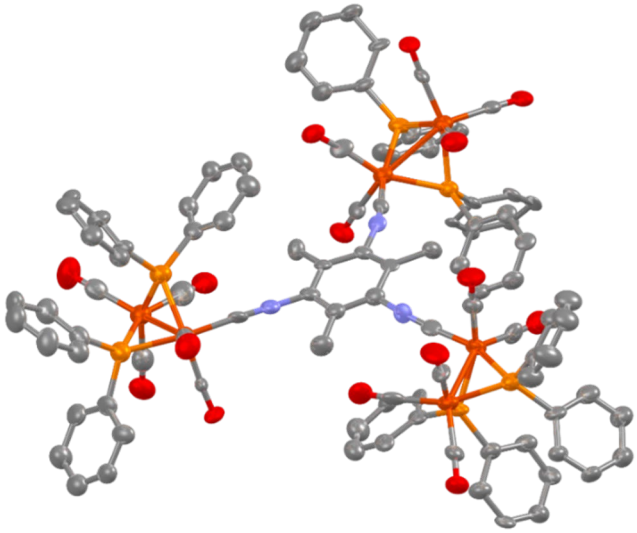

Figure 7. Molecular structure of 4 determined by single-crystal XRD. Hydrogen atoms and toluene solvent molecules are excluded for clarity.

In our initial crystallization studies, we found that complex **4** was insoluble in most alcohol solvents, in which isopropyl alcohol (IPA) was chosen as the suitable anti-solvent due to its sterically hindered structure. Promising crystallization results were achieved with combinations of IPA and acetonitrile, dimethylformamide, toluene, and benzene. Gratifyingly, crystallization by layer diffusion using toluene and IPA at 25 ℃ yielded shiny, orange single crystals. The resulting crystalline product was characterized by IR and ^{1}H NMR spectroscopy, and the molecular structure of **4** was determined by single-crystal x-ray diffraction (XRD) (**Figure 7**).

The isocyanide ligand of the synthesized complex was monitored by IR spectroscopy (**Figure 8**). The diagnostic NC and CO stretching frequencies of **1**, **2**, **3**, and **4** are listed in **Table 2**. As expected, one of the CO peaks of **1** occurred at 2055 cm^{-1} was

not observed upon coordination to the aromatic core, suggesting one terminal carbonyl has been replaced with an isocyanide ligand. This observation is consistent in all three derivatized complexes. Inspection of the IR spectra shows that the NC stretching frequency of complex **4** occurred at 2087 cm^{-1}, which is significantly lower compared to that of the free triisocyanide ligand (2111 cm^{-1}). A shift to lower wavenumbers suggests the NC ligand participates in π–backbonding while acting as a σ-donor. It is worth noting that similar discrepancies were seen in complexes **2** and **3** with smaller magnitudes of variation, indicating the presence of more $Fe_2(CO)_5(\mu -PPh_2)_2$ fragments corresponded to an increase in π–back donation.

Table 2. Diagnostic IR stretching frequencies of NC and CO for 1–4

Compound	$\nu_{C\equiv N}\ (cm^{-1})$	$\nu_{C\equiv O}\ (cm^{-1})$
1[a]	-	2055, 2015, 1991, 1964
2[a]	2109	2025, 1986, 1966, 1948
3[a]	2104	2023, 1988, 1966, 1949
4[b]	2087	2022, 1988, 1953

[a] Recorded in toluene
[b] Recorded in in CH_2Cl_2

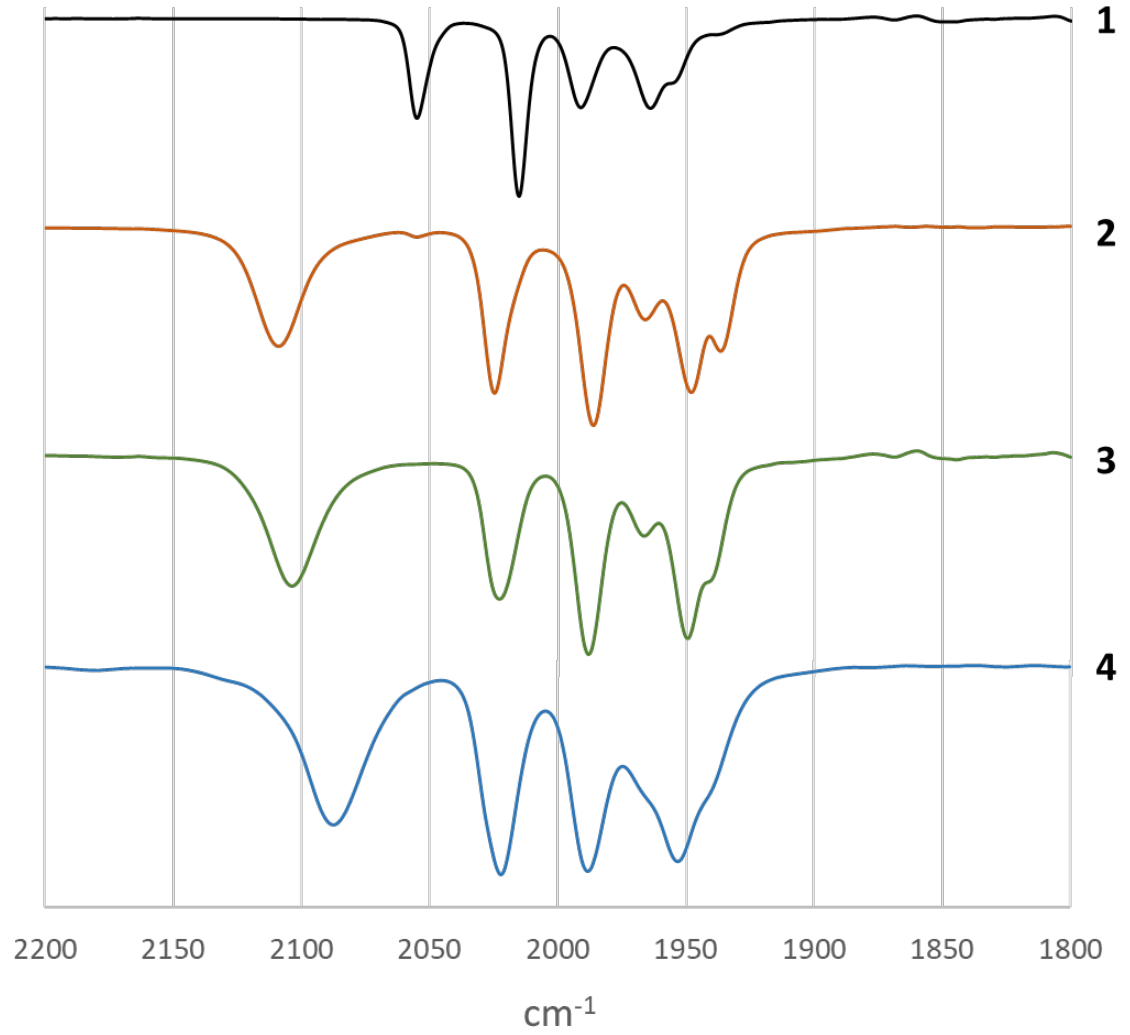

Figure 8. IR spectra of 1 – 4 showing only the diagnostic regions of NC and CO

The ^{1}H NMR spectrum of **4** displayed the expected sharp singlet at 1.68 ppm corresponding to the methyl groups on the aromatic core. Additionally, the aromatic regions on the NMR spectrum displayed several peaks representing the aromatic protons on the derivatized $Fe_2(CO)_5(\mu-PPh_2)_2$ subunit. Upon the successive replacement of a carbonyl with the weaker π–accepting **d** ligand, we expected the presence of two different electronic environments within the $Fe_2(CO)_5(\mu-PPh_2)_2$ fragments. In this context, a change in electron density due to π–backbonding resulted in differences in chemical shifts of the mentioned aromatic protons. Interestingly, diagnostic chemical shifts of toluene

were also observed, suggesting this solvent molecule is trapped within the structure of the synthesized complex. This observation is consistent with the crystallographic results, in which toluene were seen within the crystal lattice of **4**.

CHAPTER 3. ELECTROCHEMICAL STUDIES OF MOLECULAR ASSEMBLIES

3.1 Introduction

One of the primary objectives of this thesis is to explore the electron-sink behaviour of the redox-active assemblies containing multiple $Fe_2(CO)_5(\mu\text{-}PPh_2)_2$ fragments appended to an aromatic core. We were drawn to $Fe_2(CO)_6(\mu\text{-}PPh_2)_2$ (**1**) as the redox precursor for our studies due to its simple structure and convenient synthesis.[43-44] Furthermore, complex **1** is conveniently stable towards air oxidation, and the reduced dianion experience reversible oxidation when exposed to molecular oxygen.[45] Most importantly, **1** is known to undergo a reversible two-electron transfer process via two sequential one-electron reduction steps. Interestingly, the second electron transfer is thermodynamically more favourable than the first, a situation commonly referred to as *redox potential inversion*.[46-48]

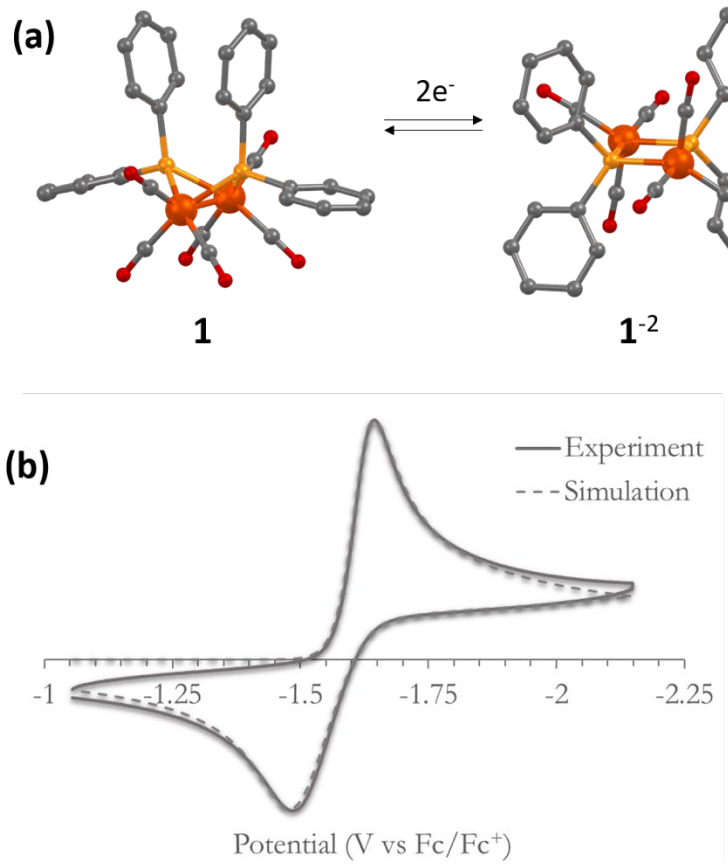

Figure 9. a) Schematic representation of structural changes of 1 upon reduction. b) Experimental (solid line) and simulated (dotted line) cyclic voltammograms of 1.

In the previous chapter, we proposed a modular synthetic approach to prepare assemblies containing one, two, and three $Fe_2(CO)_5(\mu\text{-}PPh_2)_2$ fragments. Specifically, complex **2** was first prepared to observe the spectroscopic and electrochemical changes of the $Fe_2(CO)_5(\mu\text{-}PPh_2)_2$ fragments upon replacement of a CO ligand with an isocyanide aromatic core. In our pilot electrochemical experiments, the cyclic voltammetry profile of complex **2** suggested that the arylisocyanide ligand did not alter the parent subunit's electrochemical properties. This finding further validated aromatic isocyanides are suitable ligands for the purpose of our studies. We speculated that appending more redox-active $Fe_2(CO)_5(\mu\text{-}PPh_2)_2$ fragments onto aromatic ligands would result in an expansion

in electron-sink capacity. Specifically, **3** and **4** were hypothesized to accommodate up to four and six electrons, respectively. In this chapter, the investigation of redox behaviours and electron-sink capacities of **2**, **3**, and **4** via cyclic voltammetry is discussed. Additionally, parameters such as formal potentials, charge transfer coefficients, and rate constants obtained from simulated models will also be reported herein.

3.2 Experimental

General considerations

Unless otherwise indicated, all electrochemical experiments were performed with a PARSTAT 4000A potentiostat under inert nitrogen atmosphere. Nitrogen gas was purified by passing through columns of activated copper catalyst (BASF PuriStar R3-11G) and molecular sieves (RCI-DRI 13X). Except where indicated, all chemical reagents were used as received without further purification. All solvents were dried according to standard procedures. $[Bu_4N][PF_6]$ (CHEM-IMPEX INT'L INC., 98.48 %) was purified by recrystallization using ethanol and water prior to use. DMF (Beantown Chemical, 99.9 %) were distilled under reduced pressure and stored over molecular sieves prior to electrochemical experiments according to published procedures. Glassware was dried in an oven at 130 ℃, assembled while hot, and was allowed to cool under reduced pressure.

Cyclic voltammetry

Cyclic voltammograms were recorded in 0.25 M $[Bu_4N][PF_6]$ DMF solution at varying scan rates. Glassy carbon working electrode (3 mm, CH Instruments) was used for all experiments and was polished with aqueous slurries of 0.05 μm MicroPolish alumina powder (CH Instrument, Inc.) and rinsed with Milli-Q water and methanol. The working electrode were preconditioned by performing two cyclic scans from 0.5 to 2.0 V at 0.1 mV/sec in 0.25 M DMF solution of $[Bu_4N][PF_6]$ (TBAPF6). A graphite rod counter electrode was polished and washed with methanol before use. A silver wire immersed in a 0.25 M DMF solution of TBAPF6 separated from the cell compartment by a porous glass frit (CoralPor 1000) was employed as a Ag^+/Ag pseudoreference electrode.

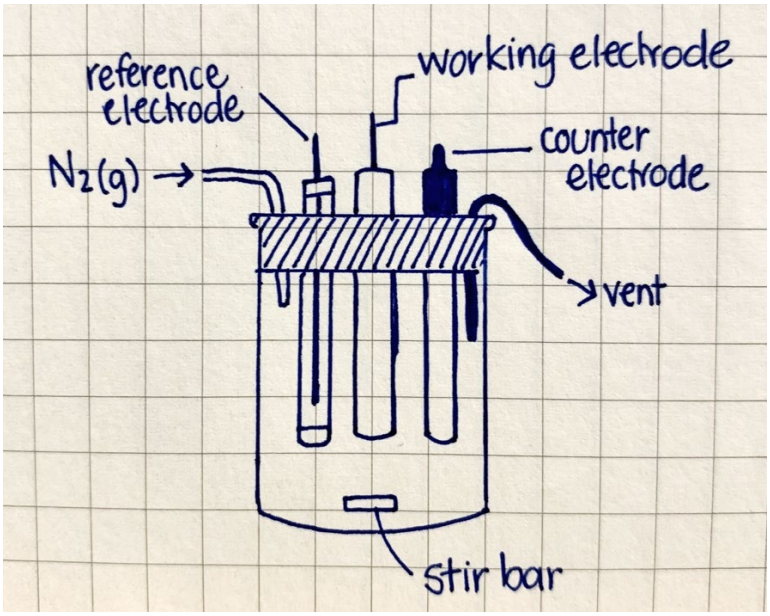

Figure 10. Schematic representation of CV experimental set up.

Cyclic voltammograms were recorded at the following rates: 0.01, 0.025, 0.05, 0.075, 0.1, 0.15, 0.25, 0.50, and 1.0 V/s. Between each scan, initial conditions at the working electrode surface were restored via polishing. iR correction was done via electrochemical impedance spectroscopy (EIS) in between scan to compensate for 90 % of solution resistance. Measured potentials are reported relative to the ferrocenium/ferrocene redox couple. Simulated kinetic parameters were optimized using a non-linear regression protocol within the DigiElch software. All simulation models assume redox potential inversion mechanisms.

Controlled Potential Electrolysis

Electrolysis in 0.25 M DMF solution of TBAPF6 was conducted at 0.5 V in the three-electrode manner. The Ag^{+}/Ag pseudoreference electrode was prepared by immersing a silver wire into a 0.25 M DMF solution of TBAPF6 separated from the cell compartment by a porous glass frit. The counter electrode was a platinum wired immersed in a solution of 3 % ferrocene in 0.25 M DMF solution of TBAPF6, and a Hg pool electrode was utilized as the working electrode. The complexes (1 mM) were electrolyzed until a constant current was achieved

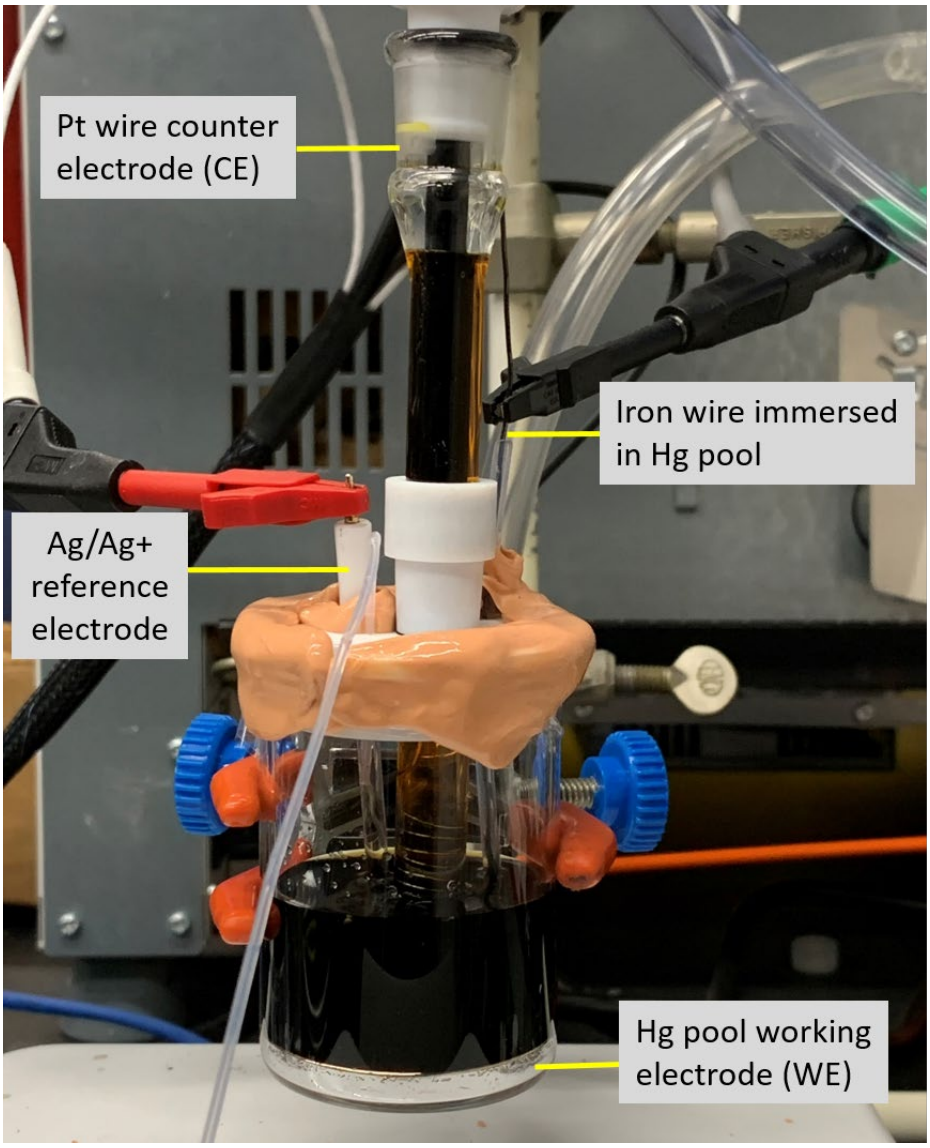

Figure 11. Controlled potential bulk electrolysis experimental set up.

3.3 Results and Discussion

Preliminary cyclic voltammetry (CV) studies were carried out in several different solvent systems at varying concentrations for complexes **1 – 4**. While some experiments yielded encouraging results, features of the cyclic voltammograms were not well resolved for complexes **3** and **4** (**Figure 12**), where peaks are expected to be more complicated. Consequently, we have designed and developed optimization conditions for complexes **1 – 4** suitable for CV analysis. Specifically, CV experiments were recorded in a 0.25 M analyte solution comprised of TBAPF6 dissolved in pure DMF. Under these conditions, CV profiles of **3** and **4** improved significantly, in which distinctive peaks on the forward reduction scans were observed.

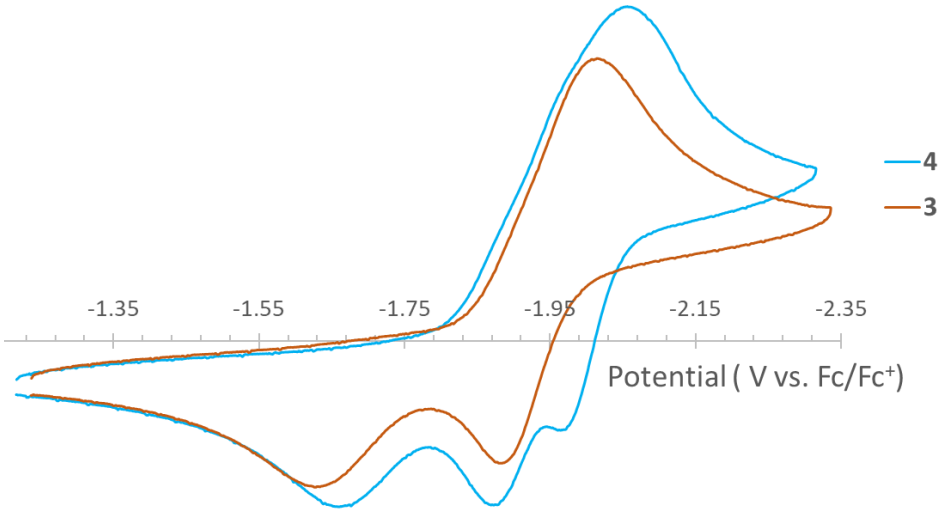

Figure 12. Experimental cyclic voltammograms of 3 and 4 recorded in 0.25 M TBAPF6 in 80:20 mesitylene:DMF solution at 0.25 V/s using glassy carbon working electrodes, graphite counter electrodes, and Ag wire pseudoreference electrodes. Features on the forward reduction scan were not well resolved, in which distinctive peaks were not observed.

Experimental and simulated cyclic voltammograms of complexes **1 – 4** under the aforementioned optimized conditions are shown in **Figure 13**. Accordingly, attachment

of one $Fe_2(CO)_5(\mu\text{-}PPh_2)_2$ fragment to a monofunctional arylisocyanide ligand, as seen in complex **2**, resulted in a cathodic shift of the redox wave relative to the parent subunit **1**. Despite such a shift in redox potentials, the derivatization did not otherwise alter the two-electron reduction capacity or the electrochemical reversibility of complex **2**. Additionally, features on CV profiles of complexes **3** and **4** were well resolved relative to previous attempts, in which additional peaks were observed.

Similar to precursor **1**, the reduction of $Fe_2(CO)_5(\mu\text{-}PPh_2)_2$ fragments was expected to occur as two one-electron transfer steps. However, CV scans of complexes **1** and **2** over a sweep rate range of 0.1 to 1.0 V/s revealed single reduction and oxidation waves. This result suggested the one-electron reactions could not be resolved due to the redox potential inversion phenomenon, which implies that the addition of the second electron is more favorable than the first. As such, the formal potential of the second electron would have a slight anodic shift relative to the first electron. Consequently, the overall process coalesced as a single peak and appeared as a single concerted two-electron transfer process. This potential inversion phenomenon was also observed in complexes **3** and **4**, where each peak maximum on the cyclic voltammograms corresponded to a two-electron reduction. Thus, complex **3** and **4** can accommodate four and six electrons, respectively. The electron-sink capacities of these complexes were further confirmed by controlled potential bulk electrolysis, in which **2**, **3**, and **4** were verified to accommodate two, four, and six electrons, respectively.

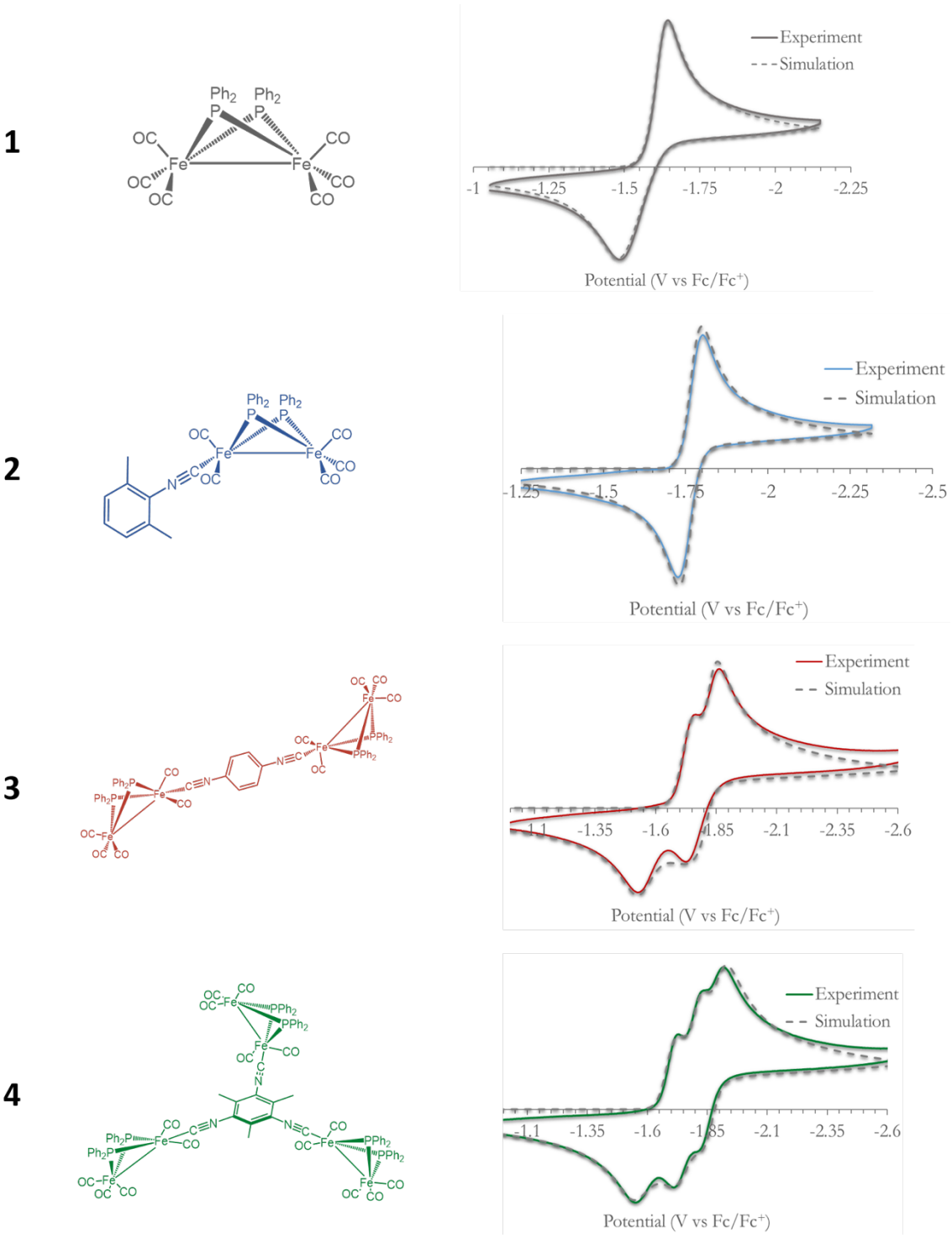

Figure 13. Schematic structures and experimental (solid lines) and simulated (dotted lines) cyclic voltammograms of complex 1 – 4 reported relative to the ferrocene redox couple. CV data recorded at 0.25 V/s scan rates are shown.

Table 3. Formal potential $E^{0\prime}$, charge transfer coefficient α, rate constant k_s, and diffusion coefficient D determined from simulated results using DigiElch.

Complex		$E^{0\prime}$ (V)	α	k_s $(cm\ s^{-1})$	D $(cm^2\ s^{-1})$
1	$\mathbf{1}^0 + e^- \rightleftarrows \mathbf{1}^{-1}$	-1.64	0.53	0.0090	3.47×10^{-6}
	$\mathbf{1}^{-1} + e^- \rightleftarrows \mathbf{1}^{-2}$	-1.52	0.40	0.0015	3.47×10^{-6}
2	$\mathbf{2}^0 + e^- \rightleftarrows \mathbf{2}^{-1}$	-1.91	0.52	0.043	2.70×10^{-6}
	$\mathbf{2}^{-1} + e^- \rightleftarrows \mathbf{2}^{-2}$	-1.61	0.48	0.040	2.70×10^{-6}
3	$\mathbf{3}^0 + e^- \rightleftarrows \mathbf{3}^{-1}$	-1.83	0.65	0.015	1.64×10^{-6}
	$\mathbf{3}^{-1} + e^- \rightleftarrows \mathbf{3}^{-2}$	-1.42	0.49	0.014	1.64×10^{-6}
	$\mathbf{3}^{-2} + e^- \rightleftarrows \mathbf{3}^{-3}$	-2.10	0.42	0.078	1.64×10^{-6}
	$\mathbf{3}^{-3} + e^- \rightleftarrows \mathbf{3}^{-4}$	-1.51	0.54	0.075	1.64×10^{-6}
4	$\mathbf{4}^0 + e^- \rightleftarrows \mathbf{4}^{-1}$	-1.81	0.55	0.014	1.82×10^{-6}
	$\mathbf{4}^- + e^- \rightleftarrows \mathbf{4}^{-2}$	-1.49	0.43	0.0052	1.82×10^{-6}
	$\mathbf{4}^{-2} + e^- \rightleftarrows \mathbf{4}^{-3}$	-1.95	0.54	0.025	1.82×10^{-6}
	$\mathbf{4}^{-3} + e^- \rightleftarrows \mathbf{4}^{-4}$	-1.63	0.49	0.011	1.82×10^{-6}
	$\mathbf{4}^{-4} + e^- \rightleftarrows \mathbf{4}^{-5}$	-2.06	0.46	0.016	1.82×10^{-6}
	$\mathbf{4}^{-5} + e^- \rightleftarrows \mathbf{4}^{-6}$	-1.70	0.47	0.023	1.82×10^{-6}

The experimental cyclic voltammogram data of complexes **1 – 4** have been modelled and fitted using DigiElch to investigate the electrochemical electron transfer processes. Parameters such as formal potentials $E^{0\prime}$, charge transfer coefficient α, rate constant k_s, and diffusion coefficient D were refined and determined using simulated CV

results. Obtained values for $E^{0\prime}$, α, k_s, and D are tabulated in **Table 3**. The charge transfer coefficients for all four complexes showed good agreements with typical values of α (approximately 0.5).[49] In complexes **1** and **2**, the formal potential of the second electron addition was more positive than the first ($E_{e2}^{0\prime} > E_{e1}^{0\prime}$), as expected for an inverted redox potential system. Similarly, the odd-electron transfer processes were shown to be more negative in complexes **3** and **4**, indicating the addition of even-electrons was more thermodynamically favorable. The results for diffusion coefficient *D* were also listed in **Table 3**, in which it was assumed that all electron transfer processes have the same diffusion coefficient as the first electron addition. Efforts had been made to optimize *D* for individual electron transfer. However, significant responses from the optimization were not observed, and the simulation was refined based on the diffusion of the first addition of electron.

The obtained rate constants k_s were also reported in **Table 3**. Despite being more thermodynamically favorable, the addition of even-electrons appeared to be slower than the odd counterparts. Upon reduction, the $Fe_2(CO)_5(\mu\text{-}PPh_2)_2$ fragment undergoes structural changes, in which the metal – metal bond was broken, and the overall structure unfolded (**Figure 9**). This structural reorganization energy, along with activation and solvent reorganization energies, was speculated to have significant impact on the kinetics of the electron transfer reactions. Thus, discrepancies in rate constants in each reduction reaction were observed.

CHAPTER 4. CONCLUSION AND FUTURE DIRECTIONS

The purpose of the experimental work described in this thesis was to demonstrate how the electron-sink capacity of molecular assemblies may be expanded. Derivatives of the redox-active precursor, $Fe_2(CO)_6(\mu\text{–}PPh_2)_2$ (**1**), were previously prepared via a modular synthetic approach to examine their electrochemical behaviours. Specifically, the simple $Fe_2(CO)_5(\mu\text{–}PPh_2)_2$ fragments were used as a common electroactive subunit and were appended to aromatic isocyanides bearing one or two functional groups. In this work, the synthesis of complex **4** was designed and reported, in which three $Fe_2(CO)_5(\mu\text{–}PPh_2)_2$ fragments were tethered to a 2,4,6-triisocyanomesitylene ligand. The structure of the resultant complex **4** was confirmed using spectroscopic and crystallographic data.

The electron-sink capacities and electrochemical properties of the derivatized complexes **2 – 4** were studied via cyclic voltammetry. Complex **2** was first prepared and analyzed as a model system to observe the effects of replacing a terminal CO functional with an isocyanide ligand. Spectroscopic and electrochemical results confirmed that no significant changes in features of the $Fe_2(CO)_5(\mu\text{–}PPh_2)_2$ fragment were observed upon derivatization, indicating isocyanide ligands are suitable for the purpose of electron-sink augmentation studies. Furthermore, under optimized experimental conditions, as evidenced by their CV profiles, the redox-active complexes **2** and **3** can accommodate up to two and four electrons, respectively. On the other hand, attaching three $Fe_2(CO)_5(\mu\text{–}PPh_2)_2$ fragments to a trifunctional arylisocyanide ligand yielded an electron-sink

ensemble **4** capable of accommodating six electrons per unit, exceeding the precedent benchmark $[Ni_{32}C_6(CO)_{36}]^{6-}$ anion.

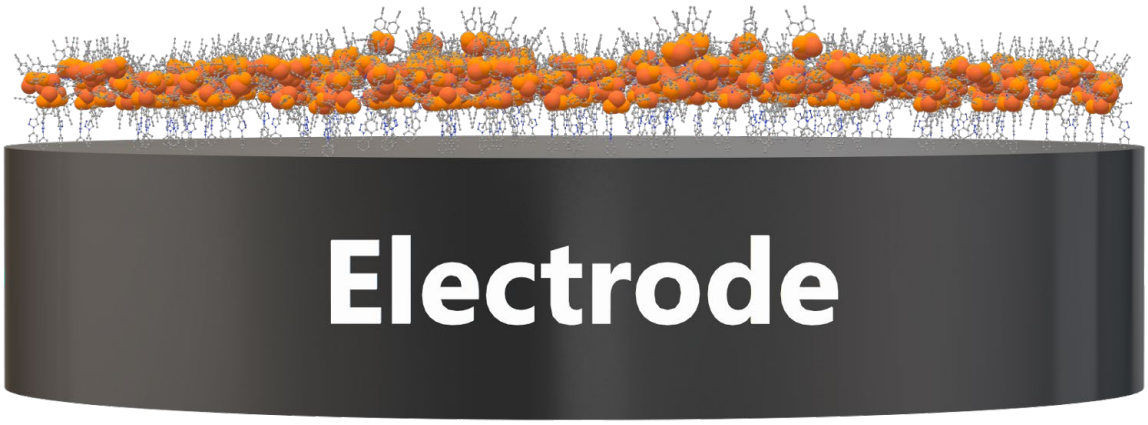

Figure 14. Schematic rendering of an electrode surface molecularly modified with the six-electron redox array 4.

Redox arrays **2 – 4** are hypothesized to contribute to an area-dependent quantum capacitance upon grafted onto electrode surfaces, where each unit of the redox-active assemblies acts as individual quantum capacitors (**Figure 14**). In this general context, the overall quantum capacitance of the electrode is determined by the electron-sink capacity of the grafted species. We further hypothesized that the overall capacitance of the electrode could be enhanced by using higher electron-sink capacity arrays, such as complex **4**. Our next step is to establish a method to graft these molecular assemblies onto electrode surfaces. Electrochemical analysis of complexes before and after tethering onto the electrode should provide valuable information regarding the electrode's mesoscopic architecture and its overall quantum capacitance.

REFERENCES

1. Dubal, D. P.; Ayyad, O.; Ruiz, V.; Gómez-Romero, P. "Hybrid energy storage: the merging of battery and supercapacitor chemistries," *Chemical Society Reviews* **2015,** *44,* 1777-1790. http://dx.doi.org/10.1039/C4CS00266K

2. Shao, Y.; El-Kady, M. F.; Sun, J.; Li, Y.; Zhang, Q.; Zhu, M.; Wang, H.; Dunn, B.; Kaner, R. B. "Design and Mechanisms of Asymmetric Supercapacitors," *Chemical Reviews* **2018,** *118,* 9233-9280. https://doi.org/10.1021/acs.chemrev.8b00252

3. Zhang, Y.; Feng, H.; Wu, X.; Wang, L.; Zhang, A.; Xia, T.; Dong, H.; Li, X.; Zhang, L. "Progress of electrochemical capacitor electrode materials: A review," *International Journal of Hydrogen Energy,* **2009,** *34,* 4889-4899.

4. Wang, G.; Zhang, L.; Zhang, J. "A Review of Electrode Materials for Electrochemical Supercapacitors." *Chemical Society Reviews,* **2012,** *41*, 797–828. https://doi.org/10.1039/C1CS15060J

5. Raza, W.; Ali, F.; Raza, N.; Luo, Y.; Kim, K.-H.; Yang, J.; Kumar, S.; Mehmood, A.; Kwon, E. E. "Recent Advancements in Supercapacitor Technology". *Nano Energy,* **2018**, *52*, 441–473. https://doi.org/10.1016/j.nanoen.2018.08.013

6. Miller, J. Introduction to electrochemical capacitor technology. *IEEE Electrical Insulation Magazine*, **2010**, *26*, 40–47. http://doi.org/10.1109/mei.2010.5511188

7. Wang, Y.; Song, Y.; Xia, Y. Electrochemical Capacitors: Mechanism, Materials, Systems, Characterization and Applications. *Chemical Society Reviews* **2016**, *45* (21), 5925–5950. http://doi.org/10.1039/c5cs00580a

8. Simon, P.; Gogotsi, Y. Materials for electrochemical capacitors. *Nature Materials*, **2008**, *7*, 845–854. http://doi.org/10.1038/nmat2297

9. Toupin, M.; Brousse, T.; Bélanger, D. Charge Storage Mechanism of MnO2Electrode Used in Aqueous Electrochemical Capacitor. *Chemistry of Materials* **2004**, *16* (16), 3184–3190. http://doi.org/10.1021/cm049649j

10. Li, L.; Zhang, Y.; Shi, F.; Zhang, Y.; Zhang, J.; Gu, C.; Wang, X.; Tu, J. Spinel Manganese–Nickel–Cobalt Ternary Oxide Nanowire Array for High-Performance Electrochemical Capacitor Applications. *ACS Applied Materials & Interfaces* **2014**, *6* (20), 18040–18047. http://doi.org/10.1021/am5048653

11. Echegoyen, L.; Echegoyen, L. E. "Electrochemistry of Fullerenes and Their Derivatives," *Accounts of Chemical Research* **1998,** *31,* 593-601. https://doi.org/10.1021/ar970138v

12. Faria, R. A. D. D.; Heneine, L. G. D.; Matencio, T.; Messaddeq, Y. Faradaic and Non-Faradaic Electrochemical Impedance Spectroscopy as Transduction Techniques for Sensing Applications. *International Journal of Biosensors & Bioelectronics* **2019**, *5* (1). http://doi.org/10.15406/ijbsbe.2019.05.00148

13. Forse, A. C.; Merlet, C.; Griffin, J. M.; Grey, C. P. New Perspectives on the Charging Mechanisms of Supercapacitors. *Journal of the American Chemical Society* **2016**, *138* (18), 5731–5744. https://doi.org/10.1021/jacs.6b02115

14. Bueno, P. R. Common Principles of Molecular Electronics and Nanoscale Electrochemistry. *Analytical Chemistry* **2018**, *90* (12), 7095–7106. https://doi.org/10.1021/acs.analchem.7b04533

15. Bueno, P. R. Nanoscale Origins of Super-Capacitance Phenomena. *Journal of Power Sources* **2019**, *414*, 420–434. https://doi.org/10.1016/j.jpowsour.2019.01.010

16. Bueno, P. R. *Nanoscale Electrochemistry of Molecular Contacts*; Springer: Cham, Switzerland, 2018.

17. Imry, Y. Mesoscopic Physics and the Fundamentals of QuantumMechanics. *Physica Scripta* **1998**, *T76* (1), 171. http://doi.org/10.1238/physica.topical.076a00171

18. Femoni, C.; Iapalucci, M. C.; Kaswalder, F.; Longoni, G.; Zacchini, S. The Possible Role of Metal Carbonyl Clusters in Nanoscience and Nanotechnologies. *Coordination Chemistry Reviews* **2006**, *250* (11-12), 1580–1604. http://doi.org/10.1016/j.ccr.2006.03.011

19. Kaniewska, K.; Ponikiewski, Ł.; Szynkiewicz, N.; Cieślik, B.; Pikies, J.; Krzystek, J.; Dragulescu-Andrasi, A.; Stoian, S. A.; Grubba, R. Homoleptic Mono-, Di-, and Tetra-Iron Complexes Featuring Phosphido Ligands: a Synthetic, Structural, and Spectroscopic Study. *Dalton Transactions* **2020**, *49* (29), 10091–10103. http://doi.org/10.1039/d0dt01503b

20. Longoni, G.; Femoni, C.; Iapalucci, M. C.; Zanello, P. "Electron-Sink Features of Homoleptic Transition-Metal Carbonyl Clusters". In Metal Clusters in Chemistry, Braunstein, P.; Oro, L. A.; Raithby, P. R., Eds. Wiley-VCH Verlag GmbH: 1999; pp 1137-1158. http://dx.doi.org/10.1002/9783527618316.ch3i

21. Rossi, F.; Zanello, P. "Electron Reservoir Activity of High-Nuclearity Transition Metal Carbonyl Clusters," Portugaliae Electrochimica Acta 2011, 29, 309-327.

22. Calderoni, F.; Demartin, F.; Fabrizi de Biani, F.; Femoni, C.; Iapalucci, M. C.; Longoni, G.; Zanello, P. "Electron-Sink Behaviour of the Carbonylnickel Clusters [Ni32C6(CO)36]6– and [Ni38C6(CO)42]6–: Synthesis and Characterization of the Anions [Ni32C6(CO)36]n– (n = 5–10) and [Ni38C6(CO)42]n– (n = 5–9) and Crystal Structure of [PPh3Me]6[Ni32C6(CO)36] · 4 MeCN," European Journal of Inorganic Chemistry 1999, 1999, 663-671. https://onlinelibrary.wiley.com/doi/abs/10.1002/%28SICI%291099-0682%28199904%291999%3A4%3C663%3A%3AAID-EJIC663%3E3.0.CO%3B2-1

23. Fabrizi de Biani, F.; Femoni, C.; Iapalucci, M. C.; Longoni, G.; Zanello, P.; Ceriotti, A. "Redox Behavior of [H6-nNi38Pt6(CO)48]n- (n = 4−6) Anions: A Series of Metal Carbonyl Clusters Displaying Electron-Sink Features," Inorganic Chemistry 1999, 38, 3721-3724. https://doi.org/10.1021/ic9813516

24. Whitmire, K. H. "Main Group–Transition Metal Cluster Compounds of the Group 15 Elements". In Advances in Organometallic Chemistry, Stone, F. G. A.; Robert, W., Eds. Academic Press: **1998**; Vol. Volume 42, pp 1-145. http://www.sciencedirect.com/science/article/pii/S0065305508605420

25. Humphrey, M. G.; Cifuentes, M. P. "Organo-transition metal cluster complexes". In Organometallic Chemistry: Volume 36, Fairlamb, I. J. S.; Lynam, J. M., Eds. The Royal Society of Chemistry: **2010**; Vol. 36, pp 182-205. http://dx.doi.org/10.1039/9781847559616-00182

26. Collman, J. P.; Rothrock, R. K.; Finke, R. G.; Moore, E. J.; Rose-Munch, F. Role of the Metal-Metal Bond in Transition-Metal Clusters. Phosphido-Bridged Diiron Carbonyl Complexes. *Inorganic Chemistry* **1982**, *21* (1), 146–156. https://doi.org/10.1021/ic00131a029

27. Shyu, S. G.; Calligaris, M.; Nardin, G.; Wojcicki, A. Reactions Leading to Formation and Cleavage of Metal-Metal and Metal-.Mu.-Phosphido Bonds in Binuclear Molybdenum and Tungsten Complexes. Structural Analyses of W2(CO)8(.Mu.-PPh2)2 and Its Two-Electron Reduction Product, [Li(THF)3]2[W2(CO)8(.Mu.-PPh2)2]. *Journal of the American Chemical Society,* **1987**, *109* (12), 3617–3625. https://doi.org/10.1021/ja00246a018

28. Cheah, M. H.; Borg, S. J.; Bondin, M. I.; Best, S. P. Electrocatalytic Proton Reduction by Phosphido-Bridged Diiron Carbonyl Compounds: Distant Relations to the H-Cluster? *Inorganic Chemistry* **2004**, *43* (18), 5635–5644. https://doi.org/10.1021/ic049746e

29. Park, S.-M.; Yoo, J.-S. Peer Reviewed: Electrochemical Impedance Spectroscopy for Better Electrochemical Measurements. *Analytical Chemistry* **2003**, *75* (21). https://doi.org/10.1021/ac0313973

30. Krukiewicz, K. Electrochemical Impedance Spectroscopy as a Versatile Tool for the Characterization of Neural Tissue: A Mini Review. *Electrochemistry Communications* **2020**, *116*, 106742. https://doi.org/10.1016/j.elecom.2020.106742

31. Bard, A. J.; Faulkner, L. R. *Electrochemical Methods: Fundamentals and Applications*; John Wiley & Sons: Hoboken, 2007.

32. Lasia, A. Electrochemical Impedance Spectroscopy and Its Applications; Springer: New York, NY, 2014.

33. Mei, B.-A.; Lau, J.; Lin, T.; Tolbert, S. H.; Dunn, B. S.; Pilon, L. Physical Interpretations of Electrochemical Impedance Spectroscopy of Redox Active Electrodes for Electrical Energy Storage. *The Journal of Physical Chemistry C* **2018**, *122* (43), 24499–24511. https://doi.org/10.1021/acs.jpcc.8b05241

34. Yu, Y. F.; Gallucci, J.; Wojcicki, A. Novel Mode of Reduction of Phosphido-Bridged, Metal-Metal-Bonded Binuclear Complexes. Synthesis and Reactivity of an Unsymmetrical Anion from Bis(.Mu.-Diphenylphosphido)Hexacarbonyldiiron [Fe2(CO)6(.Mu.-PPh2)2]. *Journal of the American Chemical Society* **1983**, *105* (14), 4826–4828. https://doi.org/10.1021/ja00352a046

35. Rahaman, A.; Gimbert-Suriñach, C.; Ficks, A.; Ball, G. E.; Bhadbhade, M.; Haukka, M.; Higham, L.; Nordlander, E.; Colbran, S. B. Bridgehead Isomer Effects in Bis(Phosphido)-Bridged Diiron Hexacarbonyl Proton Reduction Electrocatalysts. *Dalton Transactions* **2017**, *46* (10), 3207–3222. https://doi.org/10.1039/C6DT01494A

36. Leach, P. A.; Geib, S. J.; Corella, J. A.; Warnock, G. F.; Cooper, N. J. Synthesis and Structural Characterization of [Co{CN(2,6-C6H3Me2)}4]-, the First Transition Metal Isonitrilate. *Journal of the American Chemical Society* **1994**, *116* (19), 8566–8574. https://doi.org/10.1021/ja00098a017

37. Johnson, B. V.; Ouseph, P. J.; Hsieh, J. S.; Steinmetz, A. L.; Shade, J. E. Relative Bonding Characteristics of Cationic Isocyanide, Carbonyl, and Related Complexes of Iron as Determined by Moessbauer and Infrared Spectroscopy. *Inorganic Chemistry* **1979**, *18* (7), 1796–1799. https://doi.org/10.1021/ic50197a014

38. Sarapu, A. C.; Fenske, R. F. Transition Metal-Isocyanide Bond. Approximate Molecular Orbital Study. *Inorganic Chemistry* **1975**, *14* (2), 247–253. https://doi.org/10.1021/ic50144a006

39. Yu, Y. F.; Wojcicki, A.; Calligaris, M.; Nardin, G. "Synthesis and x-ray crystallographic characterization of the binuclear iron complexes cyclic $(CO)_3Fe(m\text{-}PPh_2)(h^2\text{-}(C,P)\text{-}m\text{-}CH(CN)PPh_2)Fe(CO)_3$ and cyclic $(CO)_3Fe(m\text{-}PPh_2)(h^2\text{-}(P,P')\text{-}m\text{-}Ph_2PC(CN)PPh_2)Fe(CO)_3$," Organometallics **1986**, *5*, 47-53. http://dx.doi.org/10.1021/om00132a008

40. Teramoto, Y.; Kubo, K.; Kume, S.; Mizuta, T. "Formation of a Hexacarbonyl Diiron Complex Having a Naphthalene-1,8-bis(phenylphosphido) Bridge and the Electrochemical Behavior of Its Derivatives," *Organometallics* **2013**, *32*, 7014-7024. https://doi.org/10.1021/om4006142

41. Huang, Y.-C.; Chen, H.-Y.; Chang, Y.-L.; Vasanthakumar, P.; Chen, S.-Y.; Kao, C.-L.; Wu, C. H.-Y.; Hsu, S. C. N. "Synthesis of triisocyanomesitylene β-diketiminato copper(I) complexes and evaluation of isocyanide π-back bonding," Polyhedron 2020, 192, 114828. https://www.sciencedirect.com/science/article/pii/S027753872030485X

42. Abraham, R. J.; Griffiths, L.; Perez, M. 1H NMR Spectra. Part 30: 1H Chemical Shifts in Amides and the Magnetic Anisotropy, Electric Field and Steric Effects of the Amide Group. *Magnetic Resonance in Chemistry* **2013**, *51* (3), 143–155. https://doi.org/10.1002/mrc.3920

43. Collman, J. P.; Rothrock, R. K.; Finke, R. G.; Moore, E. J.; Rose-Munch, F. "Role of the metal-metal bond in transition-metal clusters. Phosphido-bridged diiron carbonyl complexes," *Inorganic Chemistry* **1982,** *21,* 146-156. http://dx.doi.org/10.1021/ic00131a029

44. Yu, Y. F.; Wojcicki, A.; Calligaris, M.; Nardin, G. "Synthesis and x-ray crystallographic characterization of the binuclear iron complexes cyclic (CO)3Fe(m-PPh2)(h2-(C,P)-m-CH(CN)PPh2)Fe(CO)3 and cyclic (CO)3Fe(m-PPh2)(h2-(P,P')-m-Ph2PC(CN)PPh2)Fe(CO)3," Organometallics 1986, 5, 47-53. http://dx.doi.org/10.1021/om00132a008

45.

46. Cheah, M. H.; Borg, S. J.; Bondin, M. I.; Best, S. P. "Electrocatalytic Proton Reduction by Phosphido-Bridged Diiron Carbonyl Compounds: Distant Relations to the H-Cluster?," *Inorganic Chemistry* **2004,** *43,* 5635-5644. http://dx.doi.org/10.1021/ic049746e

47. Uhrhammer, D.; Schultz, F. A. "Energetics of Concerted Two-Electron Transfer and Metal−Metal Bond Cleavage in Phosphido-Bridged Molybdenum and Tungsten Carbonyl Complexes," Journal of Physical Chemistry A 2002, 106, 11630-11636. http://dx.doi.org/10.1021/jp021557z

48. Lord, R. L.; Schultz, F. A.; Baik, M.-H. "Two-Electron Redox Energetics in Ligand-Bridged Dinuclear Molybdenum and Tungsten Complexes," Inorganic Chemistry 2010, 49, 4611-4619. http://dx.doi.org/10.1021/ic100186v

49. Baik, M.-H.; Ziegler, T.; Schauer, C. K. "Density Functional Theory Study of Redox Pairs. 1. Dinuclear Iron Complexes That Undergo Multielectron Redox Reactions Accompanied by a Reversible Structural Change," Journal of the American Chemical Society 2000, 122, 9143-9154. https://doi.org/10.1021/ja993522r

50. Guidelli, R.; Compton, R. G.; Feliu, J. M.; Gileadi, E.; Lipkowski, J.; Schmickler, W.; Trasatti, S. Defining the Transfer Coefficient in Electrochemistry: An Assessment (IUPAC Technical Report). *Pure and Applied Chemistry* **2014**, *86* (2), 245–258. https://doi.org/10.1515/pac-2014-5026

APPENDIX A

NMR spectra of complex 4 2,4,6-triisocyaniomesitylene ligand, and important intermediates

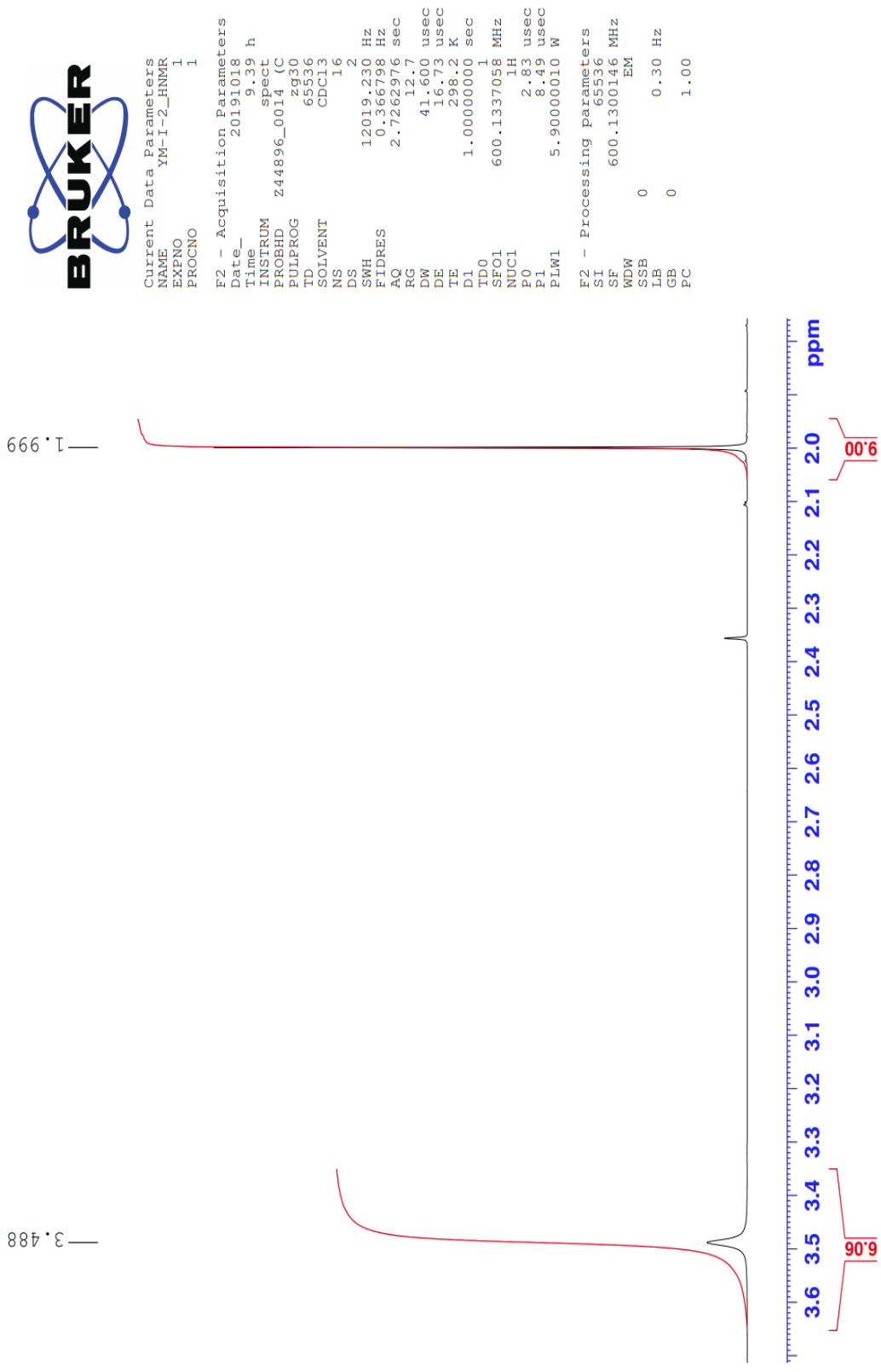

Figure S1. 1H NMR spectrum of 2,4,6-triaminomesitylene.

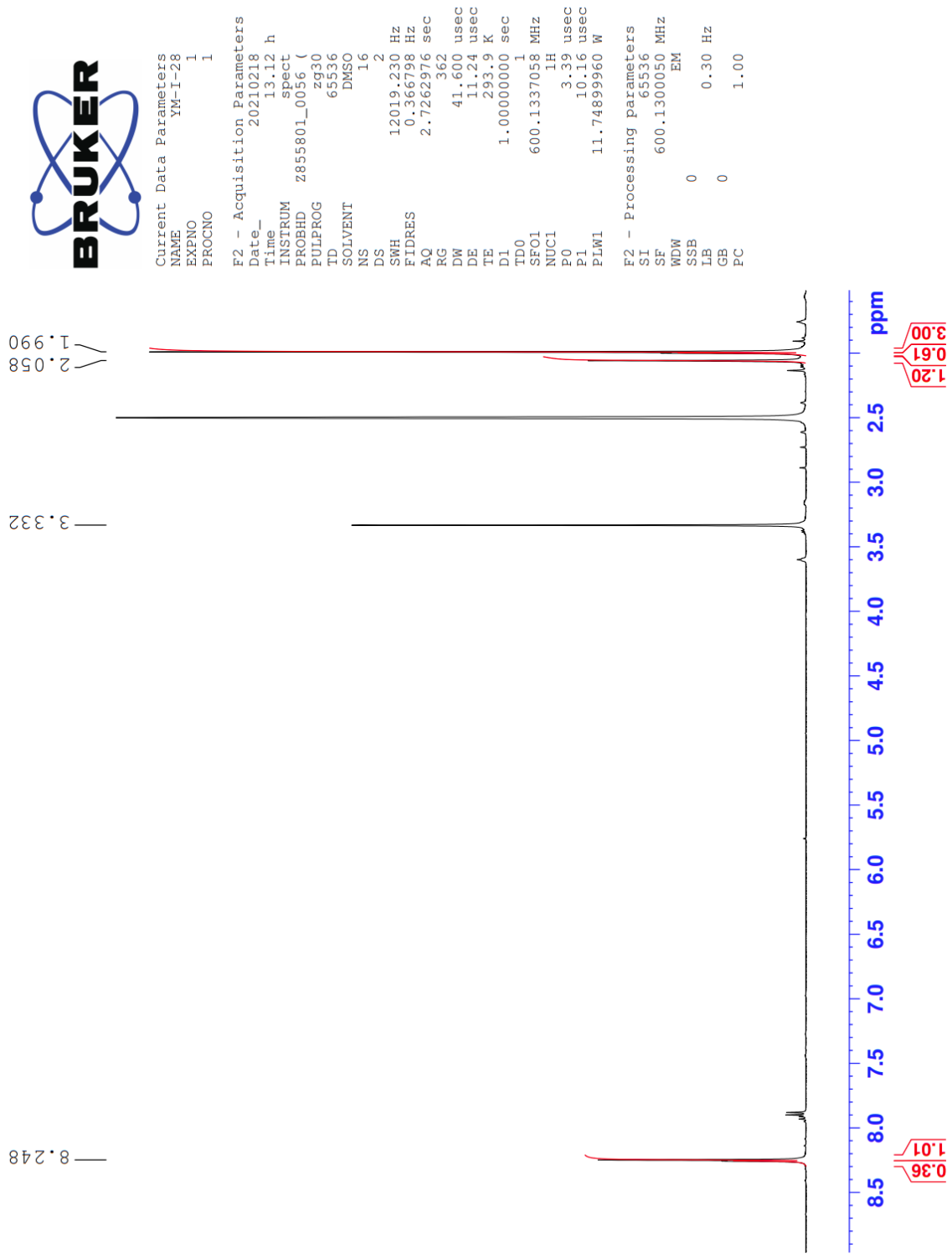

Figure S2. 1H NR spectrum of 2,4,6-triformamidomesitylene.

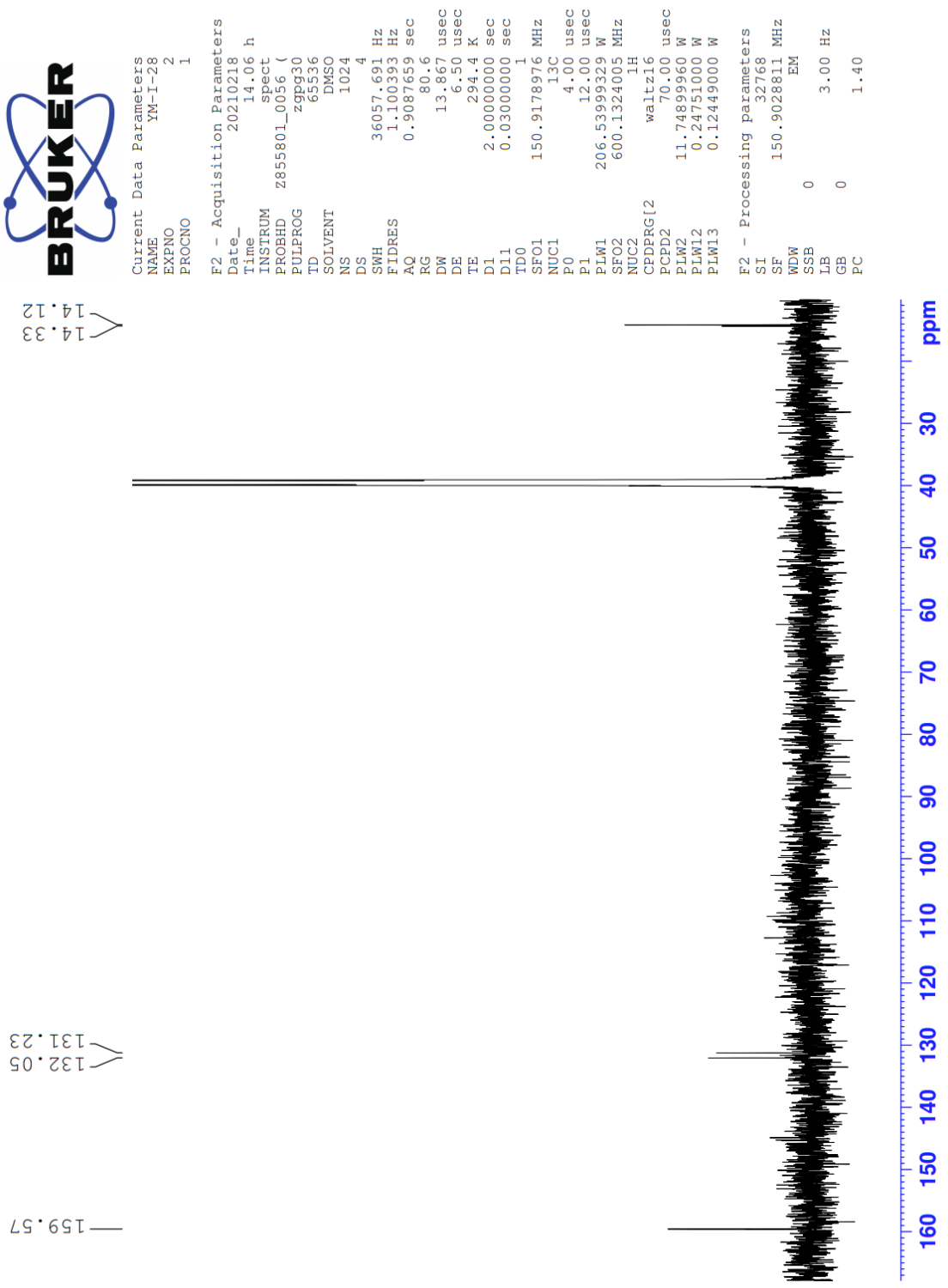

Figure S3. **^{13}C NMR spectrum of 2,4,6-triformamidomesitylene.**

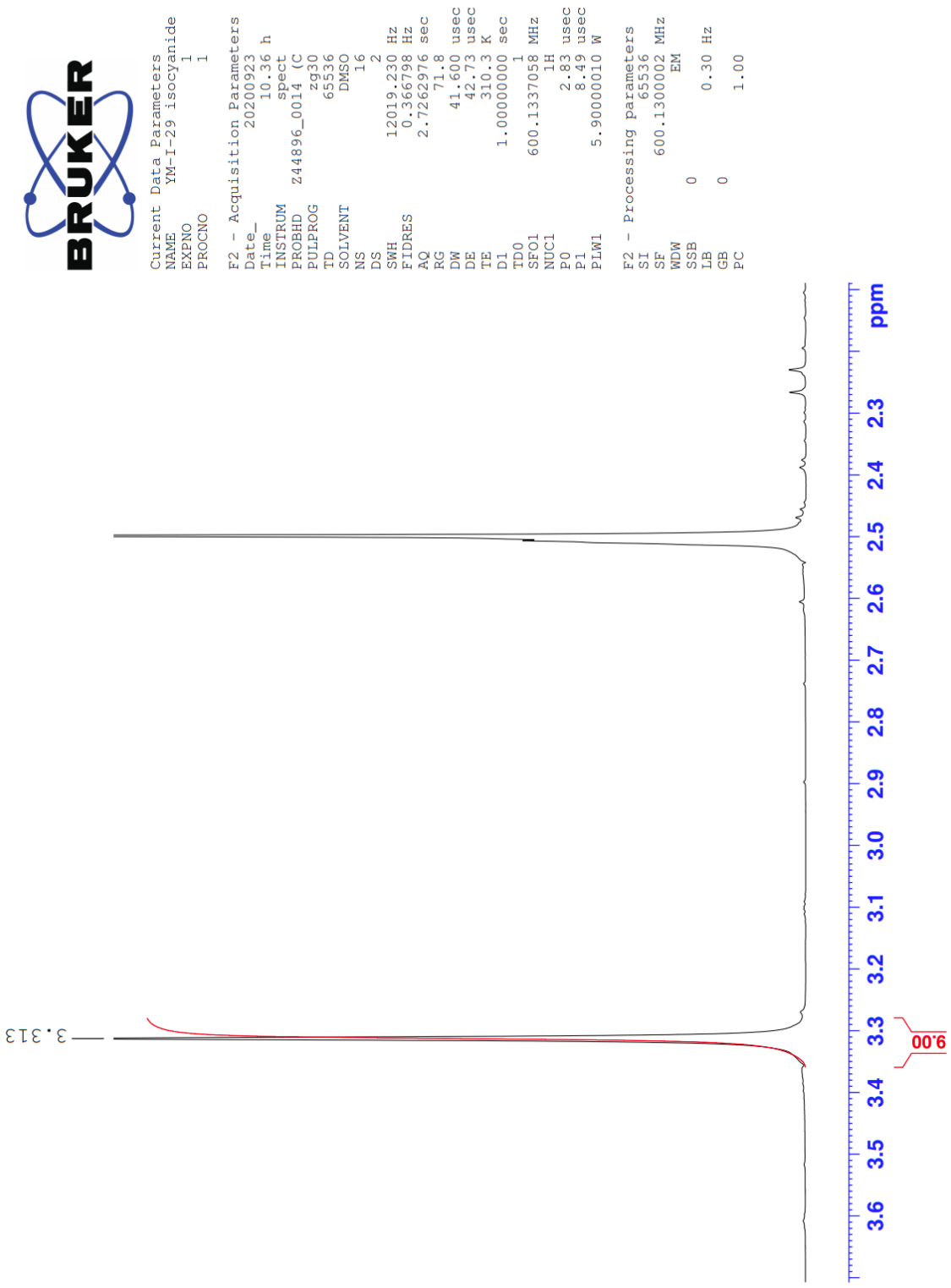

Figure S4. 1H NMR spectrum of 2,4,6-triisocyanomesitylene.

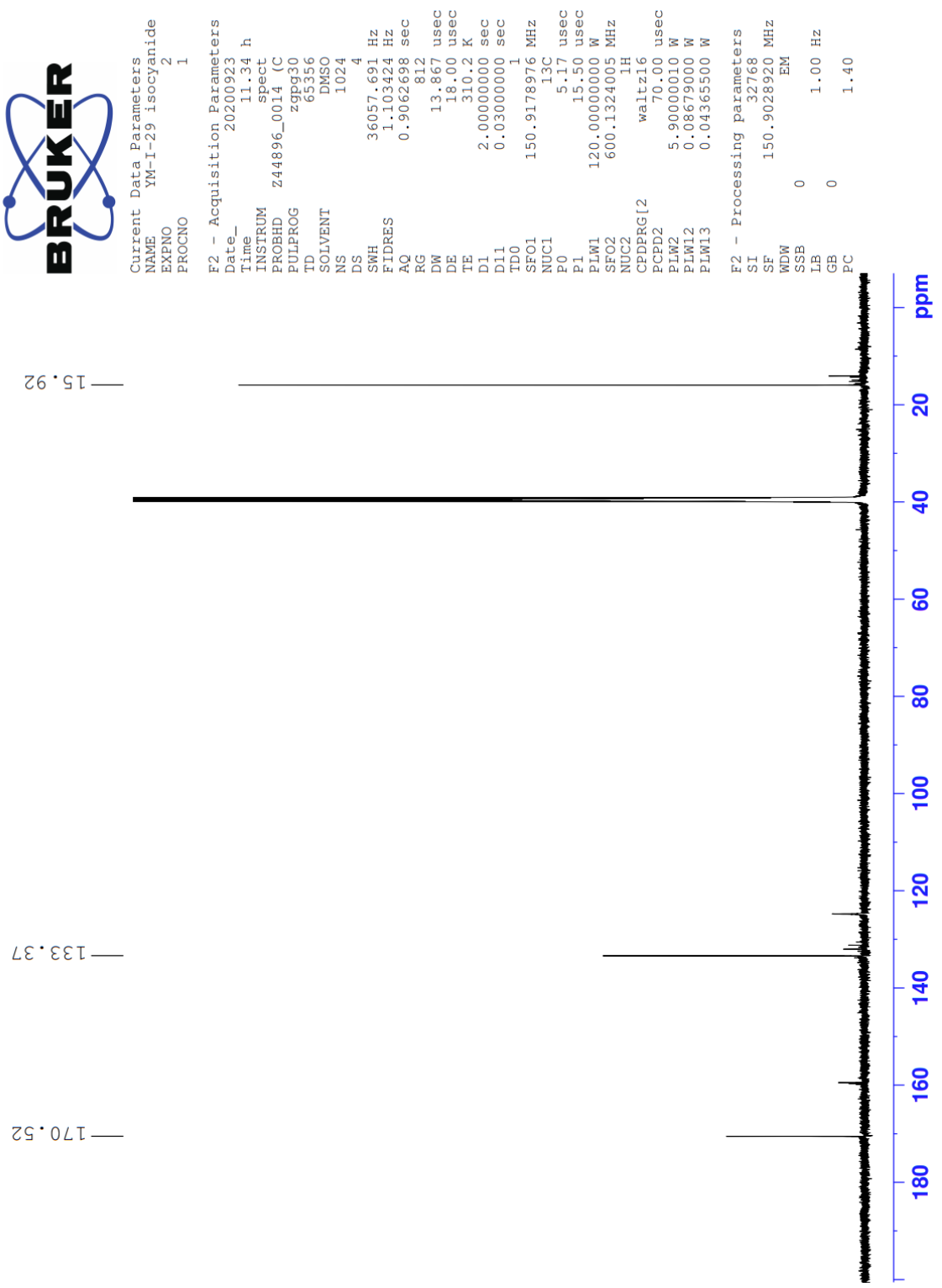

Figure S5. **^{13}C NMR spectrum of 2,4,6-triisocyanomesitylene.**

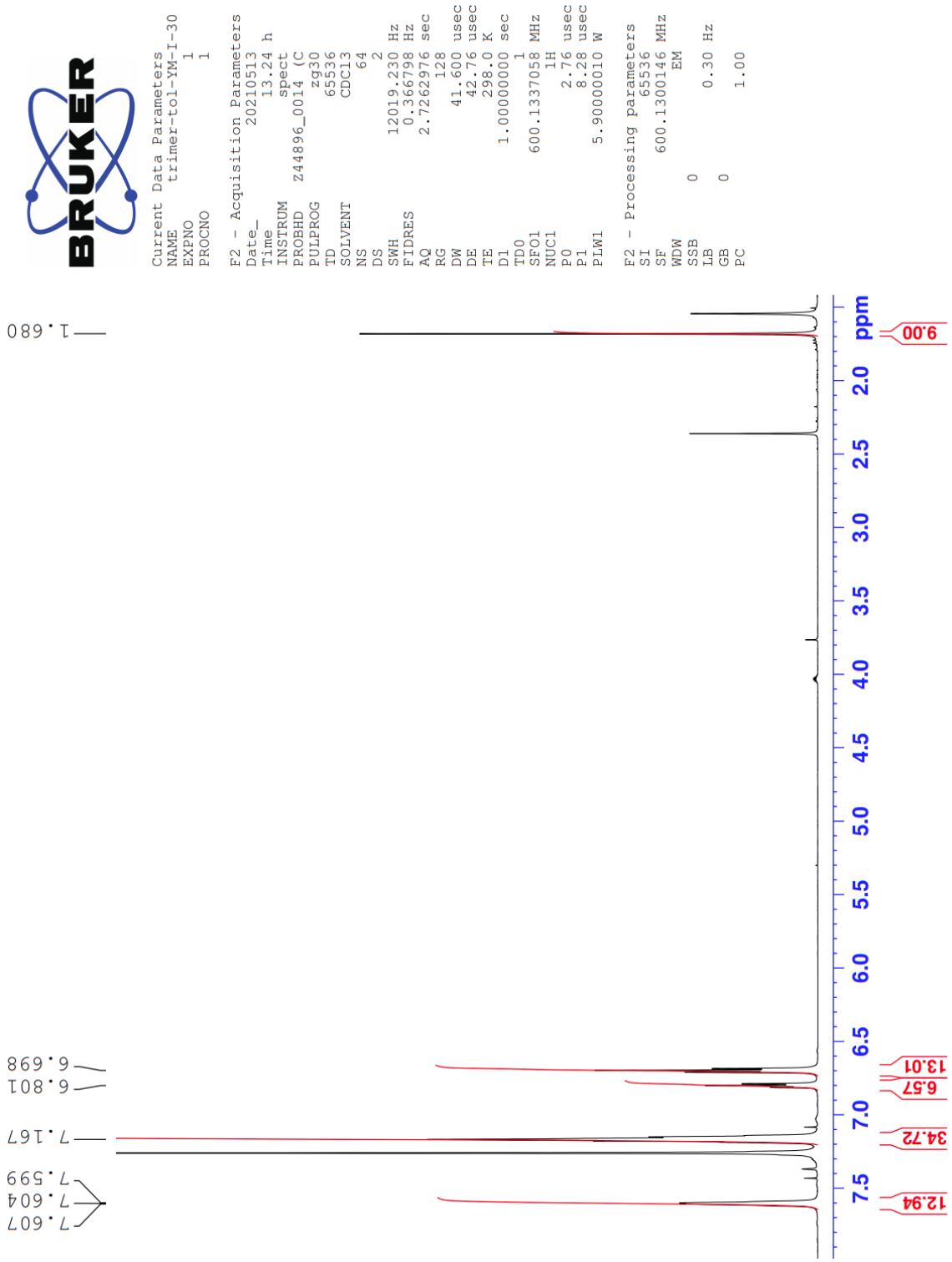

Figure S6. **^{1}H NMR spectrum of complex 4.**

Cyclic Voltammograms of complexes 2, 3, and 4 at varying scan rates

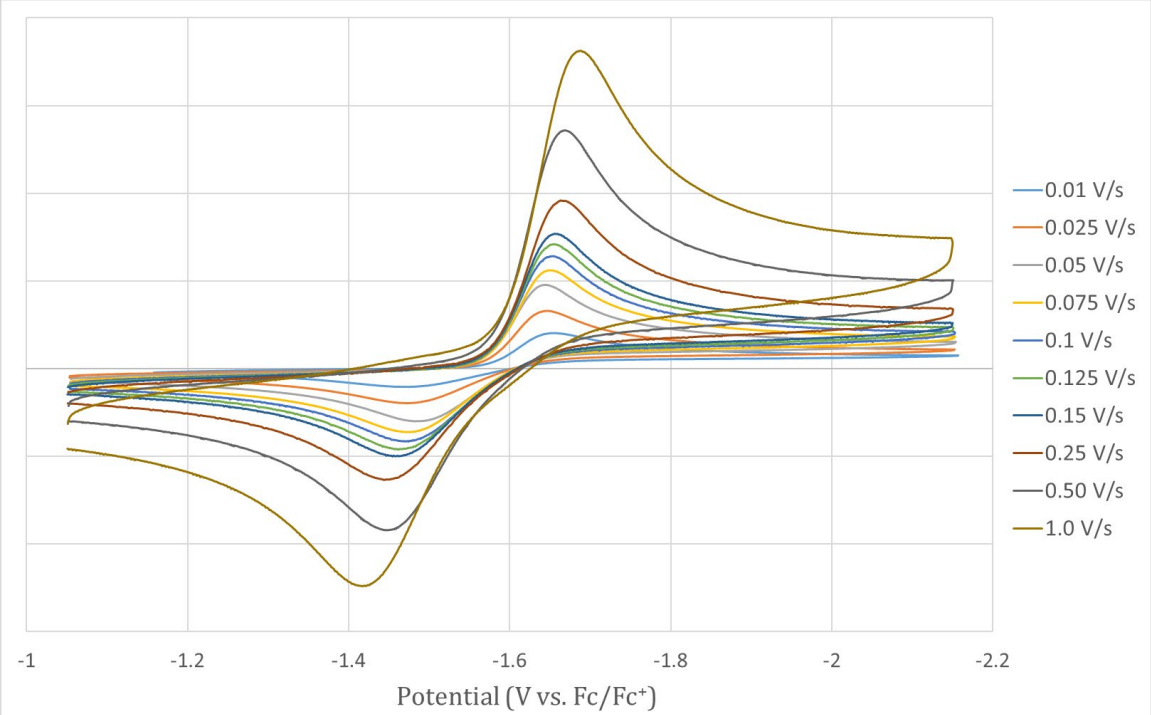

Figure S7. Cyclic voltammogram of complex 1 in 0.25 M TBAPF6 DMF solution at varying scan rates.

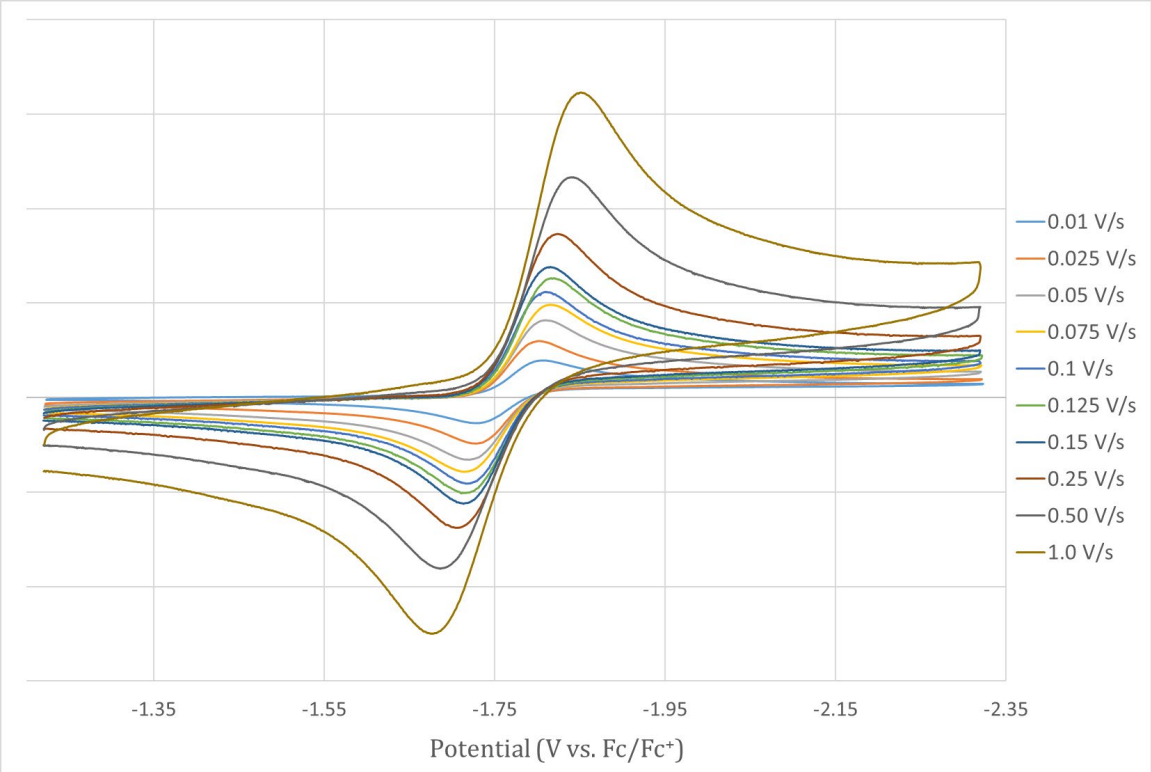

Figure S8. Cyclic voltammogram of complex 2 in 0.25 M TBAPF6 DMF solution at varying scan rates.

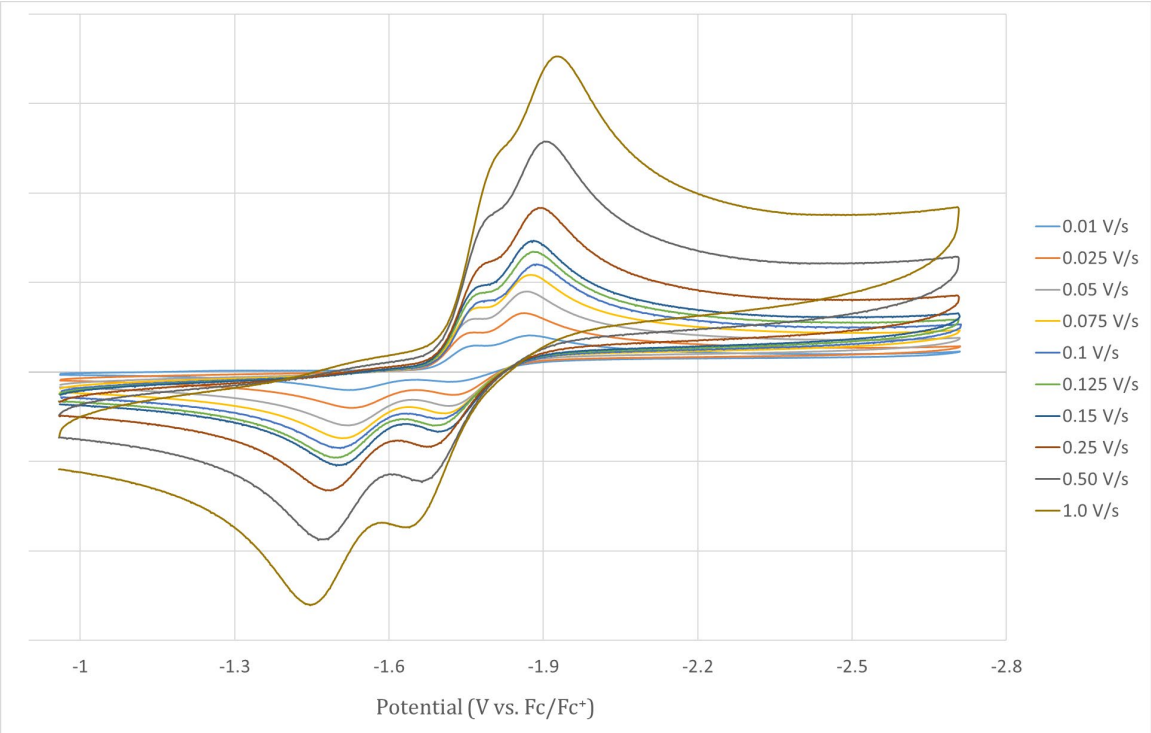

Figure S9. Cyclic voltammogram of complex 3 in 0.25 M TBAPF6 DMF solution at varying scan rates.

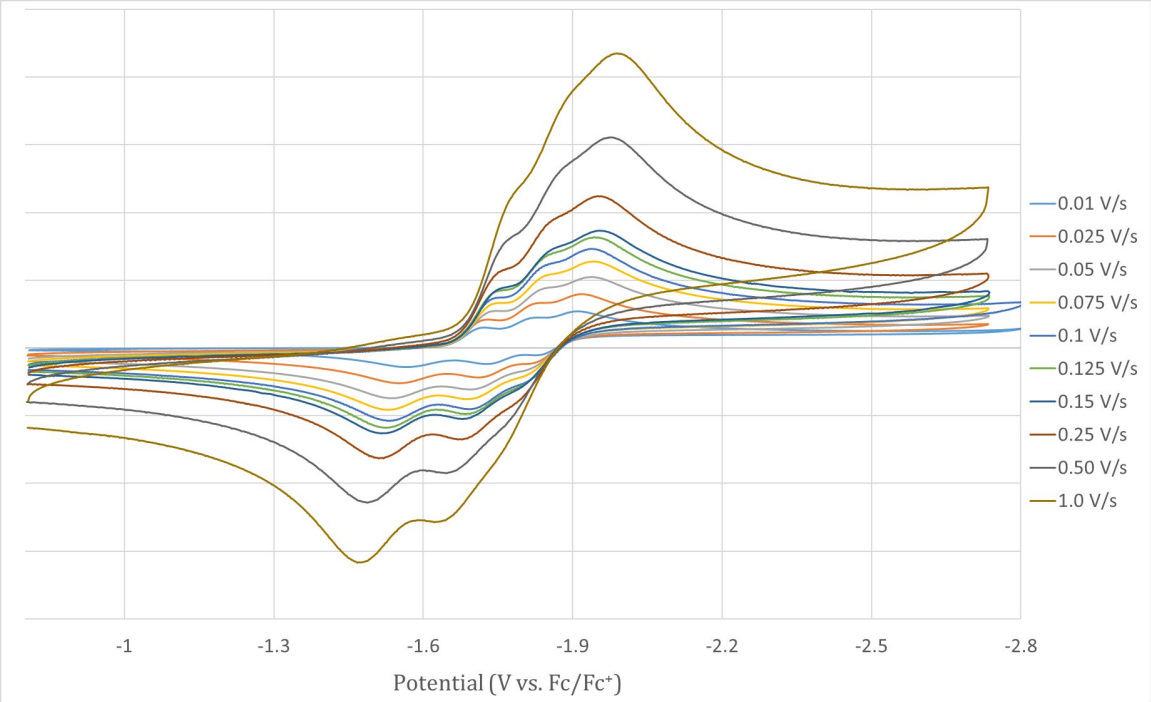

Figure S10. Cyclic voltammogram of complex 4 in 0.25 M TBAPF6 DMF solution at varying scan rates.